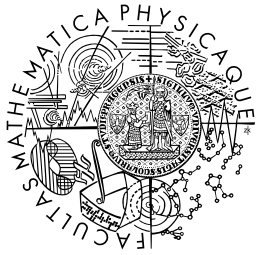

FACULTY
OF MATHEMATICS
AND PHYSICS
Charles University

BACHELOR THESIS

Martin Šípka

Gravitational collapse of scalar field

Institute of Theoretical Physics

Supervisor of the bachelor thesis: Mgr. Tomáš Ledvinka, Ph.D.
Study programme: Physics
Study branch: General physics

Prague 2017

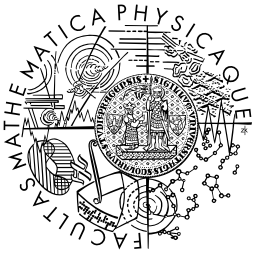

MATEMATICKO-FYZIKÁLNÍ
FAKULTA
Univerzita Karlova

BAKALÁŘSKÁ PRÁCE

Martin Šípka

Gravitační kolaps skalárního pole

Ústav teoretické fyziky

Vedoucí bakalářské práce: Mgr. Tomáš Ledvinka, Ph.D.

Studijní program: Fyzika

Studijní obor: Obecná fyzika

Praha 2017

I declare that I carried out this bachelor thesis independently, and only with the cited sources, literature and other professional sources.

I understand that my work relates to the rights and obligations under the Act No. 121/2000 Sb., the Copyright Act, as amended, in particular the fact that the Charles University has the right to conclude a license agreement on the use of this work as a school work pursuant to Section 60 subsection 1 of the Copyright Act.

In ..... date ..... 14.5.2017 signature of the author

Title: Gravitational collapse of scalar field

Author: Martin Šípka

Institute: Institute of Theoretical Physics

Supervisor: Mgr. Tomáš Ledvinka, Ph.D., Institute of Theoretical Physics

Abstract: In this thesis we study a critical collapse of a scalar field. We follow the work of [1] and create detailed and easy to understand figures and images describing the results and the phenomena observed during our calculations. We also try to give a detailed look at numerical methods used along with two ways of convergence testing.

Keywords: general relativity, critical collapse, black hole

Název práce: Gravitační kolaps skalárního pole

Autor: Martin Šípka

Ústav: Ústav teoretické fyziky

Vedoucí bakalářské práce: Mgr. Tomáš Ledvinka, Ph.D., Ústav teoretické fyziky

Abstrakt: V této práci se zabýváme kritickým kolapsem skalárního pole. Na základě [1] vytváříme detailní a srozumitelné grafy a obrázky, ilustrující získané výsledky a jevy pozorované v průběhu našich výpočtů. Také se pokoušíme poskytnout detailní pohled na numerické metody použité současně se dvěma způsoby testování konvergence.

Klíčová slova: obecná relativita, černé díry, kritický kolaps

First, I would like to express my deepest thanks to my supervisor Mgr. Tomáš Ledvinka, Ph.D. for his help that made the existence of this thesis possible. His passion for new and unknown was highly motivating and inspiring. Having someone so skilled and willing to help was crucial for my understanding of the principles of the general relativity and one of its most complex and fascinating phenomenom - critical collapse.
I musn't forget my family and friends without whom I would never be able to write these words. My mom and my father for leading me the right way even when I did not see it. My roommates for changing every minor obstacle to a joke to laugh at and many others that made the time spent with my studies an enjoyable journey.

Contents

Introduction **2**

1 Gravitational collapse of a scalar field **3**
1.1 Gravitational collapse . . . 3
1.2 Critical collapse . . . 3
1.3 Carter-Penrose and phase diagrams . . . 4

2 Geometry and coordinates **7**
2.1 Basic equations . . . 7
2.2 Coordinates . . . 7
2.3 Wave equation . . . 8
2.4 Compactification . . . 9

3 Numerical Methods **11**
3.1 Grid . . . 11
3.1.1 Geodesics calculation . . . 11
3.2 Diamond integral scheme . . . 12
3.2.1 Solving the geodesics equation to get the required timestep Δu . . . 12
3.2.2 Evaluating the integral . . . 13
3.3 Hypersurface equations calculation . . . 13
3.4 Initial data . . . 14
3.5 Bisection search . . . 15

4 Convergence tests **17**
4.1 Test for data at $\mathscr{I}^+$ . . . 17
4.2 Convergence for small time u . . . 19
4.3 Testing with Einstein equations . . . 19

5 Near-critical data **21**
5.1 Behaviour for small p . . . 21
5.2 Above-critical evolution . . . 24
5.3 Near-critical evolution . . . 27
5.3.1 Bisection search results . . . 27
5.3.2 Below-critical solution . . . 29
5.3.3 Above-critical solution . . . 32
5.4 Phase diagram . . . 35
5.5 Self-similarity . . . 37

Conclusion **39**

List of Figures **40**

Bibliography **43**

Introduction

The main goal of this thesis is to study a gravitational collapse of a scalar field, with a focus put on a critical behaviour near to a black hole creation threshold. We are following the approach and using mostly the equations from [1]. Apart from reproducing their results, we try to give a detailed explanation of the numerical methods and algorithms used, the thing missing in the article. The convergence tests of the numerical methods are also the part of this thesis, confirming the second order of our algorithm. The real error of the calculations is tested with the remaining unused Einstein equations.

Another important thing we tried to focus on were the phase diagrams, the way of describing a collapsing matter evolution using an analogy of a trajectory in a phase space. With appropriate coordinates we tried to construct such diagram and show that the critical solution attractor is not a point, rather a curve in a phase space.

To better understand the coordinates we choose to display some of the figures in the Carter-Penrose diagrams. We first describe the diagram and its structure and then we use them for results plotting.

In the chapter about the results of our work we first try to introduce the reader how a weak scalar field behaves in the spacetime. Then we study the creation of a black hole with large mass and radius. Afterwards we find the solution closest to the critical one, where the black hole is not created. We describe the solution focusing on the critical phenomena. The slightly above-critical solution is also presented. With this solution we observe the late black hole creation, and its properties.

1. Gravitational collapse of a scalar field

1.1 Gravitational collapse

A gravitational collapse is a process in which a matter concentrates due to its own gravity. In space it is a basic process responsible for formation of galaxies, star systems, planets and other structures present in the universe. General relativity permits the creation of objects called black holes. A black hole is a spacetime region not even the light can escape [2]. A black hole can have various size and mass. We will try to show that theoretically very small black holes can exist. Since a black hole does not emit any observable light it cannot be seen directly with a telescope. Other, more sophisticated methods have been developed, mostly being dependent on how a matter near a black hole behaves, in order to find and study these mysterious objects. Theoretical calculations and numerical simulations should be able to help us understand a black hole creation and its behaviour.

1.2 Critical collapse

In 1993 Choptuik [3] studied a gravitating massless scalar field in the Einstein's theory of gravity and found number of interesting phenomena. He focused on black hole formations, choosing family of initial data characterized by a parameter p. He then varied the parameter and observed the evolution of the system. He found a critical point p^* where an infinitesimal change in p results either in formation of a black hole or in the field being dispersed to infinity. He observed a relation between $p - p^*$ and a final mass of a black hole, meaning a black hole of arbitrary mass can be created. His work has been later adapted by others, working not only with a scalar field, but with a model closer to reality including the perfect fluid [4]. A charged scalar field was also studied by Gundlach and Martín-García [5] showing the scaling law for a charge of a black hole similar to the one for mass.

As mentioned in the previus section a black hole of arbitrary mass can be created if p approaches p^*. Black hole mass is then scaled as:

$$M \propto (p - p^*)^\gamma, \tag{1.1}$$

where γ is the exponent that depends only on the type of matter used, not on what we choose as our parameter p. For a massless scalar field the exponent $\gamma \approx 0.373$ [1]. A similar law can also be formulated for scaling of a black hole's charge in a charged field collapse:

$$Q \propto (p - p^*)^\delta. \tag{1.2}$$

The exponent δ has the same properties as γ mentioned above. It is only dependent on the type of matter used, not the choice of the initial data family.

The critical solution displays a type of symmetry called self-similarity. A spacetime in certain region look almost the same on different scales. We will be observing this feature and with appropriate figures demonstrate that regions on different scales are self-similar.

While in this thesis we focus on the simplest situation, that the spherical symmetry definitely is, it cannot be used for calculations where an angular momentum is present. Therefore, a significant amount of research is now focused on the axial symmetry. See for example work of Choptiuk [6]. The rotating model where spherical symmetry could not be a factor to simplify the equations and the calculations was also successfully modeled in 2016, with similar results, showing black holes display the type of behaviour described above even with matter initially rotating [7].

1.3 Carter-Penrose and phase diagrams

To better understand the causality in our spacetime, we are using compactified figures called Carter-Penrose diagrams (see e.g. [2] for details). In the spherical symmetry these represent $t-r$ hyperplane of a spacetime with specific coordinates in which

- radial null geodesics are 45-degree lines
- infinite radii are by an appropriate transformation put into a point with finite space coordinate, all radiation thus ends at so-called null infinity $\mathscr{I}^+$.
- If the spacetime contains a horizon, it is plotted as a 45-degree line separating those outgoing null rays which hit $\mathscr{I}^+$ and those which (however much trying to be outgoing) end up in a singularity.

As we study a massless scalar field with its wave packets propagating with the speed of light, these diagrams can make our results more understandable. In our simulations we also use a null coordinate u and lines of $u = const$ which not only represent the radial outgoing null worldline, but also form the hypersurface where our initial data are given. Such diagrams are thus a natural tool for plotting the results. Using these diagrams, we can better understand features of both geometry and fields. An example of such diagram is shown in the Figure 1.1.

Another approach to explain the character of a critical collapse is using an analogy of a trajectory in a phase space. Our phase space is composed of all possible initial data. It has therefore an infinite number of dimensions. The trajectories are then composed of the points that together form the time evolution of a system. This means the lines should not cross, since we are solving the evolution equations. In [8] the phase diagrams shown in figures 1 and 2, the attractors are fixed points. We have found them to be curves in a phase space as is mentioned in [12], for the situation when the discrete self-similarity is present in the critical solution.

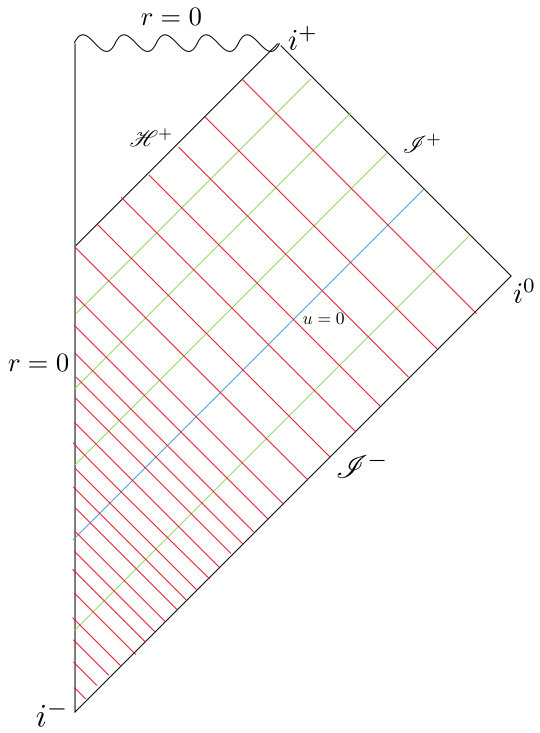

Figure 1.1: A Penrose diagram of a collapse adapted from [1]. The green lines are $u = const$ slices of the constant retarded time u. We are using the retarded time also for our simulations. The blue lines represent $x = const$ hypersurfaces. $\mathscr{H}^+$ is the the event horizon. $\mathscr{I}^+$ serves as a symbol for the future null infinity that all null rays above the horizon reach, while $\mathscr{I}^-$ is the past null infinity. Singularity inside a black hole horizon is shown with the wavy line. The blue line $u = 0$ is where we set the initial data and let them evolve.

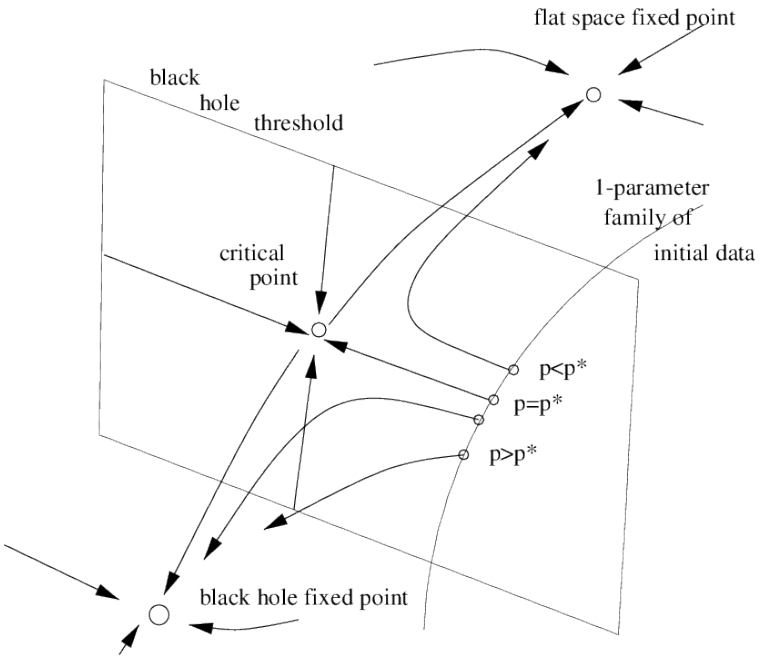

Figure 1.2: Phase diagram from [8]. The figure descibes expected trajectories in a phase space from a number of initial states. The curve made by varying p and keeping other parameter constant is marked. The point p^* is the black hole threshold, from which the system ends up in the critical point. The hyperplane representing all points that lead the evolution to the critical point is $\infty - 1$ dimensional and is also shown in the figure (as a 2D plane). The points representing black hole formation and flatspace are two other possible ending states for our system. A system having any initial data parameter non-critical necessarily ends in either of those two points, not in a critical state.

2. Geometry and coordinates

2.1 Basic equations

Geometry of our spacetime must satisfy Einstein equations:

$$R_{ab} - \frac{1}{2}Rg_{ab} + \Lambda g_{ab} \equiv G_{ab} + \Lambda g_{ab} = 8\pi T_{ab}. \tag{2.1}$$

In this work we are using a sign convention proposed by [2]. These famous equations were formulated by Einstein in 1915. The role of a variable we are solving for, belongs the the metric g_{ab}, a second-order symmetrical tensor, while R_{ab} and R is Ricci tensor and Ricci scalar, build from the field and its first and second derivatives. We should note, we put $\Lambda = 0$. Our stress-energy tensor is for a massless scalar field ϕ:

$$T_{ab} = \nabla_a\phi\nabla_b\phi - \frac{1}{2}g_{ab}\nabla_a\phi\nabla_b\phi. \tag{2.2}$$

We choose a massless scalar field because of one particular reason - It satisfies the wave equation:

$$\Box_g\phi = 0. \tag{2.3}$$

So while it is quite hard to imagine how such an entity looks like, it is the simplest object which can play a role of a collapsing matter. Also, because the field is massless, no scale at which a black hole creation can occur is present. These are the reasons why Choptuik has chosen a massles scalar field for his pioneering work with a critical collapse.

2.2 Coordinates

In our numerical models we will be assuming a spherical symmetry, since this model has been extensively studied in the past. As we wish to reproduce the results of [1] and study fields up to infinity we get Bondi's coordinates as a natural choice. Bondi Coordinate system contains u as a retarded time variable and $\{r, \phi, \theta\}$ to describe the $u = const$ hypersurface. More about Bondi coordinate system in [9]. In all our calculations we use a metric defined by a line element:

$$ds^2 = -e^{2\beta(u,r)}du\Big(\frac{V(u,r)}{r}du + 2dr\Big) + r^2(d\theta^2 + sin^2\theta dr^2). \tag{2.4}$$

where we require a regular center at $r = 0$. Next we require our metric to be smooth, which results in the requirement at β and V/r to be the smooth functions on the spacetime manifold. The metric functions behave as:

$$\begin{aligned} \beta(u_0, r) &= \mathcal{O}(r^2), \\ V(u_0, r) &= r + \mathcal{O}(r^3) \end{aligned} \tag{2.5}$$

in the center of symmetry. These conditions are necessary to be followed while constructing our algorithm.

2.3 Wave equation

First we introduce a rescaled scalar field variable $\psi = \phi r$. This is a common approach in the spherical symmetry. This means, that:

$$\psi = \mathcal{O}(r), \tag{2.6}$$

since the source-free field ϕ has to be finite at the center. In terms of a new variable ψ as described in [10] we get:

$$\Box_h \psi - \left(\frac{V}{r}\right)_{,r} \frac{e^{-2\beta}\psi}{r} = 0. \tag{2.7}$$

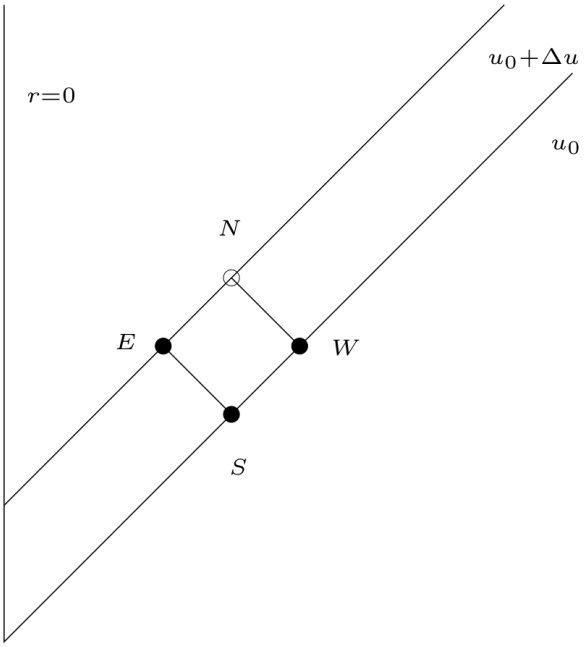

Figure 2.1: So-called marching algorithm for the wave equation. The value at vertex N is computed using (2.16) from already known values at E, S and W. This way the data at the new $u = const$ slice are obtained.

$$\int_\Sigma \Box_h \psi = \int_\Sigma \left(\frac{V}{r}\right)_{,r} \frac{\psi}{r}. \tag{2.8}$$

We follow [1] where it is shown, that the curved-space wave operator in (2.3) can be rewriten using flat 1+1 d'Alembert operator since all two-dimensional manifolds are conformally related. In such situation a standard marching algorithm

for solving flat 1+1 wave equation can be used (see Fig 2.1). Here it takes form of:

$$\psi_N = \psi_W + \psi_E - \psi_S - \int_\Sigma \left(\frac{V}{r}\right)_{,r} \frac{\psi}{r}. \tag{2.9}$$

Note this results were derived without actually using the Einstein equations (2.1). When examining the Einstein equations we get from (r, r) and (u, r) component of the equations the conditions for derivatives of β and V:

$$\begin{aligned} V_{,r} &= e^{2\beta}, \\ \beta_{,r} &= 2\pi r(\phi_{,r})^2. \end{aligned} \tag{2.10}$$

We will be using a mass function m called Misner-Sharp mass-function defined as:

$$m(u, r) = \frac{r}{2}\Big[1 - \frac{V}{r}e^{2\beta}\Big]. \tag{2.11}$$

In general relativity it is surprisingly non-trivial to define a function responsible for total energy present in a closed space. Misner and Sharp [11] studied gravitational collapse in spherical symetry and showed that in the sphere of radius r, the total energy of the matter and field can be expressed by (2.11). Apart from providing us with information about black hole mass, more advantages of this function will be clear in the next section.

2.4 Compactification

In general relativity it is common to compactify the coordinate system so we can cover $r = \infty$. We will follow the work of [1] and use the coordinate x defined as:

$$x = \frac{r}{r+1}. \tag{2.12}$$

This means $x = 0$ at $r = 0$ and $x = 1$ at $r = \infty$. First we transform the equations for $\beta_{,r}$ and $V_{,r}$ to x:

$$\begin{aligned} V_{,x} &= \frac{e^{2\beta}}{(1-x)^2}, \\ \beta_{,x} &= 2\pi x(1-x)(\phi_{,x})^2. \end{aligned} \tag{2.13}$$

We can see the problem at $x = 1$ i.e. problem at infinity. We solve it by replacing V with m in our algorithm. We then get two completely regular equations:

$$\begin{aligned} \frac{dm}{dx} &= 2\pi x^2\Big[1 - \frac{2(1-x)}{x}m\Big](\phi_{,x})^2, \\ \beta_{,x} &= 2\pi x(1-x)(\phi_{,x})^2. \end{aligned} \tag{2.14}$$

The behaviour of these functions in the origin is:

$$\begin{aligned} \beta(u, x) &= \mathcal{O}(x^2), \\ m(u, x) &= \mathcal{O}(x^3). \end{aligned} \tag{2.15}$$

We can now transform the wave equation in terms of x coordinate and the mass-function m. The equation (2.9) changes to:

$$\psi_N = \psi_W + \psi_E - \psi_S - \int_\Sigma du\, dx\, e^{2\beta} m\psi \frac{1-x}{x^3}. \tag{2.16}$$

We want our gridpoints to fall along null radial geodesics, meaning they satisfy the geodesics equation from [1]:

$$\frac{dx}{du} = -\frac{1}{2}(1-x)^2 e^{2\beta}\Big(1 - 2m\frac{1-x}{x}\Big). \tag{2.17}$$

This gives us a complete set of equations needed to simulate a gravitational collapse of a scalar field.

3. Numerical Methods

3.1 Grid

For our calculations we follow [1] and use a grid composed of points on constant retarded time u slices. A radial coordinate x of the points is calculated during runtime so that the points freely fall along the null radial geodesics, obeying the geodesics equation (2.17).

3.1.1 Geodesics calculation

The equation (2.17) is solved first for any point with $u > 0$. The equation is non-linear in x. Another compliaction is that β and m are not yet calculated. For the flat-space the geodesics curves are shown in the 3.1 Figure. For nonzero β and m we have to first approximate their values and then try to get the most accurate result possible for our new x. Our method consist of two steps. First, we use Euler method to calculate approximate x coordinate for our new gridpoint. Lets call our calculated coordinate x_a. The Euler scheme is as follows:

$$x_a^{k+1} = x^k + \Delta u f(\beta^k, m^k, x^k). \tag{3.1}$$

Note that the k is a space index. Function f is the right-hand side of the

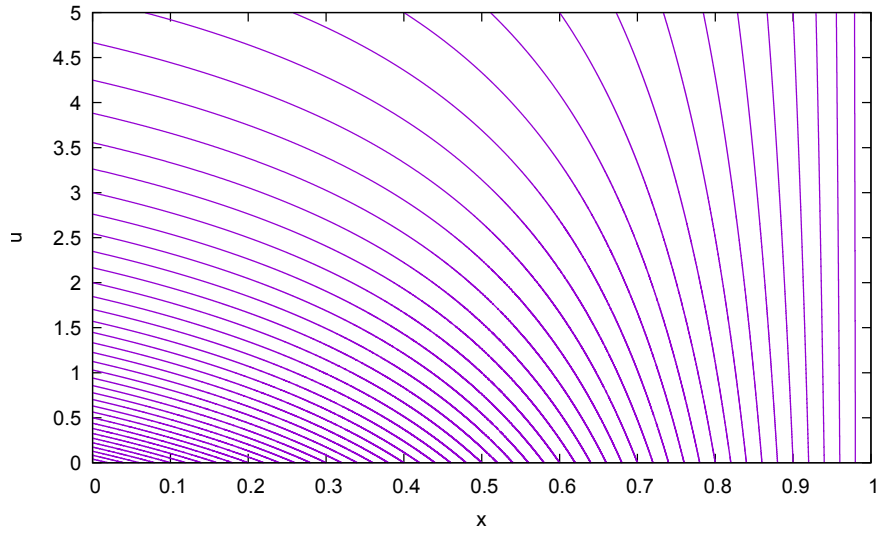

Figure 3.1: Flat-space null ingoing geodesics.

equation (2.17). Now we introduce the correction:

$$x^{k+1} = x^k + \Delta u f(\beta^{k+\frac{1}{2}}, m^{k+\frac{1}{2}}, x^{k+\frac{1}{2}}). \tag{3.2}$$

The calculation of $x^{k+\frac{1}{2}}$ is straight-forward from the formula:

$$x^{k+\frac{1}{2}} = \frac{x_a^{k+1} + x^k}{2}. \tag{3.3}$$

β and m are not yet calculated on $k+1$ point of the grid. We therefore use a simple first-order extrapolation of the values defined as follows:

$$f(x^{k+1}) = f(x^k) + \frac{f(x^k) - f(x^{k-1})}{x^k - x^{k-1}}(x^{k+1} - x^k). \tag{3.4}$$

Now we have the value approximated in the $k+1$th and kth point of the grid and it is possible to use the arithmetic mean as the value in the middle of the geodesics curve $\beta^{k+\frac{1}{2}}$ and $m^{k+\frac{1}{2}}$. The use of points x^{k-1} gives us a problem at the point one step from the center of the symmetry. There we cannot use the extrapolation method and have to adjust the scheme. However since $\beta = \mathcal{O}(x^2)$ and $m = \mathcal{O}(x^3)$ in the origin, we can approximate them by zero. We calculate the x coordinates for all the gridpoints on our next $u = const$ slice and then we proceed with ψ evaluation.

3.2 Diamond integral scheme

Using the equation (2.9) we can march through the grid calculating ψ_N using three gridpoints with already known values of ψ. When data on the hypersurface $u = const$ are known and we assume $\psi = 0$ at $x = 0$ we can calculate the timestep Δu from the (2.17) so that the first point with non-zero x on the previous $u = cost$ slice has now $x = 0$ (described in the next section) and automatically $\psi = 0$. This means we always have the value on the southern, the western and the eastern gridpoint as shown in 2.1 from [1].

3.2.1 Solving the geodesics equation to get the required timestep Δu

Since the equation (2.17) contains β and m and we are close to $x = 0$ we approximate them by zero. This simplifies the equation to:

$$\frac{dx}{du} = -\frac{1}{2}(1-x)^2\, du\,. \tag{3.5}$$

We then continue with simplification, setting also x^2 term from the bracket as zero. This gives us the final form o the equation in the center as:

$$\frac{dx}{du} = -\frac{1}{2} + x. \tag{3.6}$$

So the next timestep u is calculated as:

$$u = u_0 + \frac{2x}{x-1}. \tag{3.7}$$

Where u_0 is previous timestep.

3.2.2 Evaluating the integral

We are calculating the integral (2.16) on the area bounded by two parallel $u = const$ hypersurfaces and two generally non-straight lines defined by (2.17). We use the values of β, m, ψ and x in the middle calculated as:

$$f_m = \frac{f_E + f_W}{2}. \tag{3.8}$$

Note we cannot use f_N value of neither β, ψ nor m since these are not calculated yet. The integral can then be rewritten as:

$$\begin{aligned} \int_\Sigma dudx e^{2\beta} m\psi \frac{1-x}{x^3} \approx e^{2\beta_m} m_m \psi_m \frac{1-x_m}{x_m^3} \int_\Sigma dudx \approx \\ \approx e^{2\beta_m} m_m \psi_m \frac{1-x_m}{x_m^3} S, \end{aligned} \tag{3.9}$$

where we assume S is a trapezoid in $x-u$ coordinates, whose area we calculate as:

$$S = \frac{(x_N - x_W + x_E - x_S)\Delta u}{2}. \tag{3.10}$$

Now after we have ψ_N evaluated, we can proceed with the calculation of β and m on the northern gridpoint.

3.3 Hypersurface equations calculation

Solving of the hypersurface equations is done after we have already found ψ in the x^{k+1} gridpoint. To numerically get the radial derivative of ϕ used in (2.13) we can then use the scheme:

$$\phi_{,x}^{k+\frac{1}{2}} = \frac{\phi^{k+1} - \phi^k}{x^{k+1} - x^k}. \tag{3.11}$$

Where the field ϕ is ψ/r. This can be written as:

$$\phi = \frac{\psi(1-x)}{x}. \tag{3.12}$$

since $r = x/(1-x)$. Using this scheme gives us a problem in the center, where $x = 0$. However, by using the condition (2.6) we can see that by deriving the Taylor series of ψ at $x = 0$ we directly get $\psi_{,x}(0) = \phi_{,x}(0) = 0$. This serves well as a first approximation of $\phi_{,x}(x^{\frac{1}{2}}) = 0$. The differentiation scheme defined above is second order accurate, thus satisfying our target to get the globally second order accurate algorithm. Equation for β is now complete and ready to use. In our code we calculate β outside the center as:

$$\beta(x^{k+1}) = \beta(x^k) + \Delta x \; 2\pi x^{k+\frac{1}{2}}(1 - x^{k+\frac{1}{2}})(\phi_{,x}^{k+\frac{1}{2}})^2. \tag{3.13}$$

Equation for m requires a little more work since m is also present in its derivative.

However from writing the similar equation than the one above for m:

$$m(x^{k+1}) = m(x^k) + \Delta x\ 2\pi(x^{k+\frac{1}{2}})^2\Big(1 - \frac{2(1-x)}{x}\Big[\frac{m^{k+1}+m^k}{2}\Big]\Big)(\phi_{,x}^{k+\frac{1}{2}})^2, \quad (3.14)$$

we can see that since dm is linear in m we can write m^{k+1} explicitly as:

$$m(x^{k+1}) = \frac{m(x^k) + 2\pi x^{k+\frac{1}{2}}(x^{k+\frac{1}{2}} - (1-x^{k+\frac{1}{2}})m(x^k))\Delta x(\phi_{,x}^{k+\frac{1}{2}})^2}{1 + 2\pi(1-x^{k+\frac{1}{2}})x^{k+\frac{1}{2}}\Delta x(\phi_{,x}^{k+\frac{1}{2}})^2}. \quad (3.15)$$

This will be our final formula for calculating m.

3.4 Initial data

We use the initial data defined at constant $u = 0$ slice. To compare the result we use the identical data as [1]. They have a form of a standard gaussian wave packet defined as:

$$\phi(u_0, x) = Ar(x)^2 exp\Big[-(\frac{r(x) - r_0}{\sigma})^2\Big], \quad (3.16)$$

where by changing the amplitude A we can strengthen or weaken the field, thus giving more or less energy to the system. The wave amplitude is the parameter p mentioned in the chapter 1.2. It is then necessary to calculate the hypersurface equations on this $u = 0$ slice. We will be using the second order accurate Runge-Kutta midpoint method described in section 3.3. The initial data are visualised in the Figure 3.2.

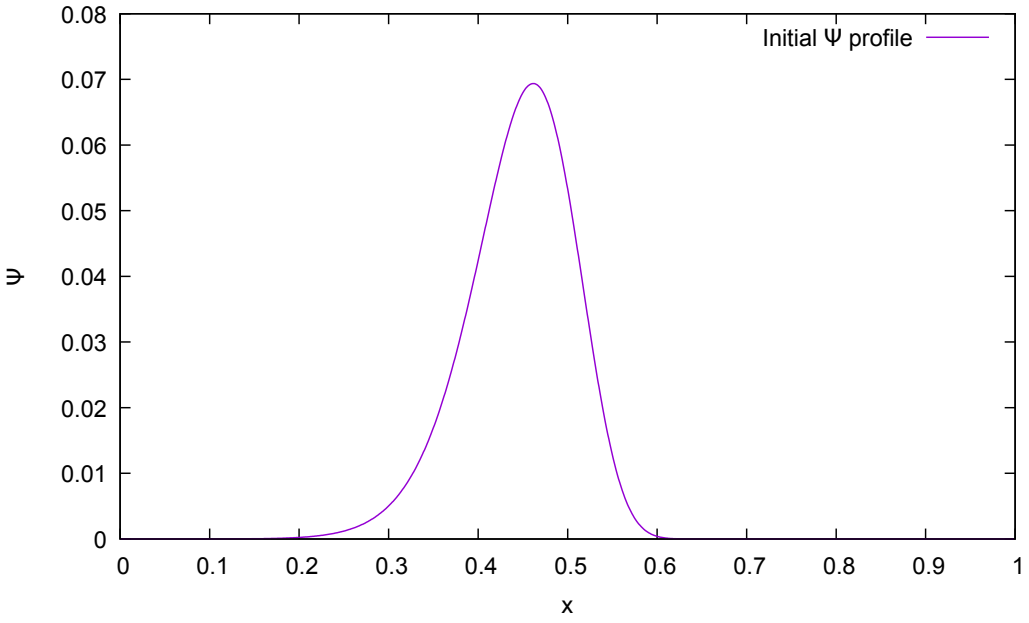

Figure 3.2: Profile of initial gaussian wave packet. Various initial data differ only by the amplitude A.

Values of β and m on the $u = 0$ slice are on the Figure 3.3.

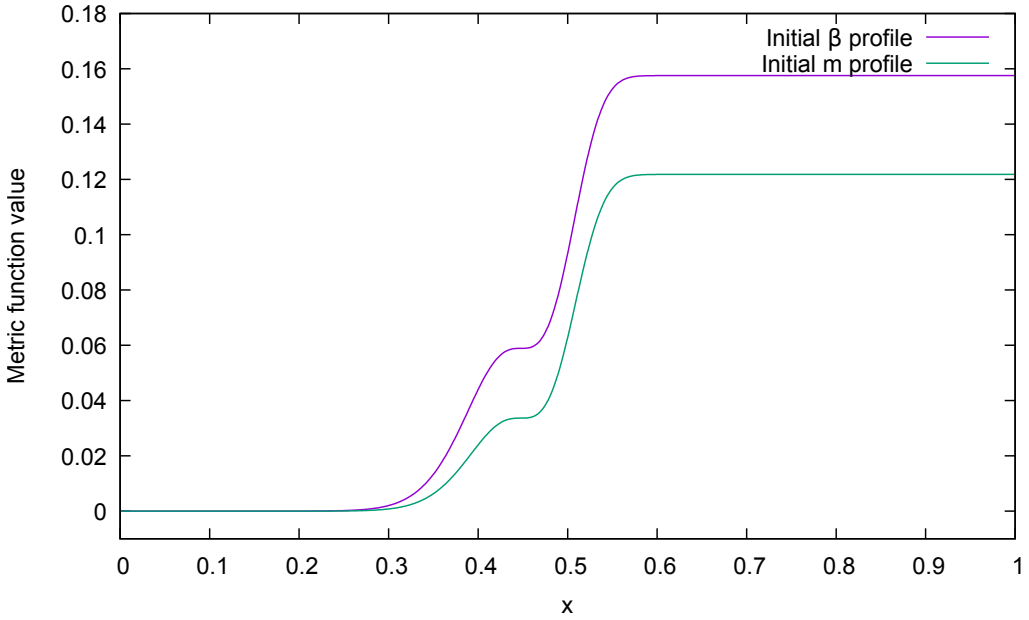

Figure 3.3: Values of metric functions beta and m in $u = 0$ slice.

In terms of r coordinate the figures are shown in 3.4 and 3.5. Note that r coordinate diverges in $x = 1$. Therefore we set the r range to [0, 6].

3.5 Bisection search

Critical parameter p^* is found using a bisection search. This is a very simple algorithm, halving the error at each step. In out case we choose the the initial minimal p_{min} and the maximal p_{max}, so that we expect the result to be in the interval $I = (p_{min}, p_{max})$. We then solve the problem for:

$$p_{mid} = \frac{p_{max} + p_{min}}{2}. \tag{3.17}$$

If a black hole was found we set $p_{min} = p_{mid}$. We set $p_{max} = p_{mid}$ otherwise. We then repeat this cycle until we get $\varepsilon = p_{max} - p_{min}$ small enough. p^* lies in this interval. In our calculations we usually expected $\varepsilon \approx 10^{-10}$ to be satisfactory. Question arises, how do we know if a black hole is present. It turns out once the value of:

$$\frac{2m}{r} > 0.65, \tag{3.18}$$

a horizon will form inevitably in a few timesteps. This way of detecting a black hole horizon is mentioned in [1] and we present a figure illustrating the $2m/r$ behaviour in the Section 5.3.1.

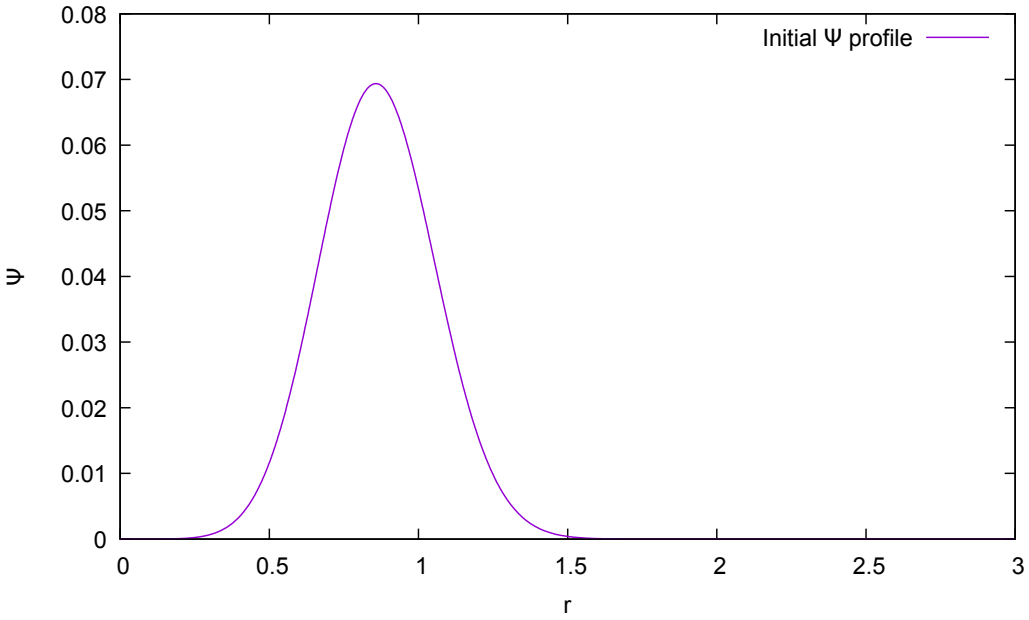

Figure 3.4: Profile of the initial gaussian wave packet in terms of r coordinate.

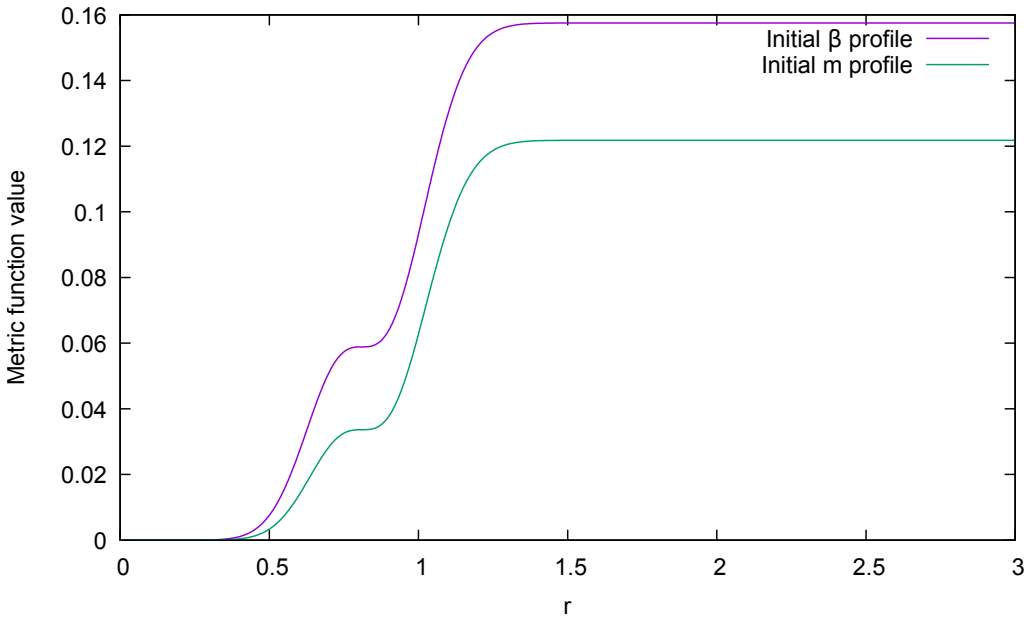

Figure 3.5: Values of the metric functions beta and m in $u = 0$ slice in terms of r coordinate.

4. Convergence tests

Important part of our thesis is a convergence test of the numerical methods used. In this chapter we will describe three methods. First one is a simple convergence test on data at $\mathscr{I}^+$. Second test is made on data in small time u. Finally we can check if the remaining Einsteins equations, we did not use in out simulation, are satisfied.

4.1 Test for data at $\mathscr{I}^+$

We have previously stated that the numerical methods are globally second order accurate. To support this claim, we observe our data at $x = 1$ slice, equivalent to $r = \infty$ or simply at $\mathscr{I}^+$. We run the standard test in which we first calculate the task for full resolution grid (if calculating ψ lets call the result ψ_h) and then halve the number of gridpoints (ψ_{2h}). Then we repeat the same, but assuming the full grid has the resolution of $2h$. We obtain ψ_{2h} and ψ_{4h}. Lets now derive how to get the order of a method directly from this kind of data. We assume the numerically calculated ψ_h has the following relation to the exact result:

$$\psi = \psi_h + h^n e. \tag{4.1}$$

Where e is an error constant for all h-s. Now for $2h$:

$$\psi = \psi_{2h} + (2h)^n e. \tag{4.2}$$

Subtracting (4.1) from (4.2) gives us:

$$\psi_{2h} - \psi_h = ((2h)^n - h^n)e. \tag{4.3}$$

For our second data pair:

$$\psi_{4h} - \psi_{2h} = ((4h)^n - (2h)^n)e. \tag{4.4}$$

Dividing the last two equations finally yields:

$$\frac{\psi_{4h} - \psi_{2h}}{\psi_{2h} - \psi_h} = \frac{((4h)^n - (2h)^n)e}{((2h)^n - h^n)e} = 2^n. \tag{4.5}$$

We can optionally logarithm the equation and get n directly:

$$n = \log_2 \Big(\frac{\psi_{4h} - \psi_{2h}}{\psi_{2h} - \psi_h} \Big). \tag{4.6}$$

We run the test for weak data, meaning we choose $p = 0.01$: less than tenth of p^*. We do this, because we are testing the numerical methods in conditions when the Einstein equations are well satisfied. We cannot guarantee the correct

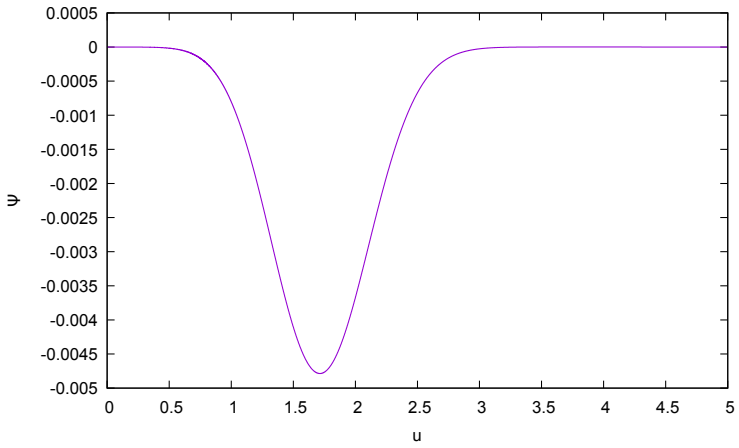

Figure 4.1: Wave profile at $\mathscr{I}^+$.

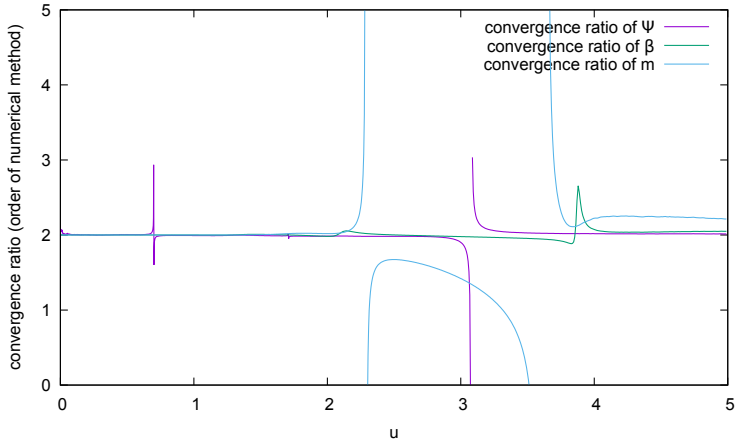

Figure 4.2: Convergence diagrams at $\mathscr{I}^+$.

result for the near-critical data. The critical phenomena appear in small scales, when too close to the criticality, possibly even on the scales smaller than our grid resolution, thus creating large numerical errors. First, we plot the ψ at $\mathscr{I}^+$ in the Figure 4.1. The convergence diagrams for ψ, m, and β are in the Figure 4.2. We have chosen to compute n from (4.6) and therefore we plot the orders of the numerical method used.

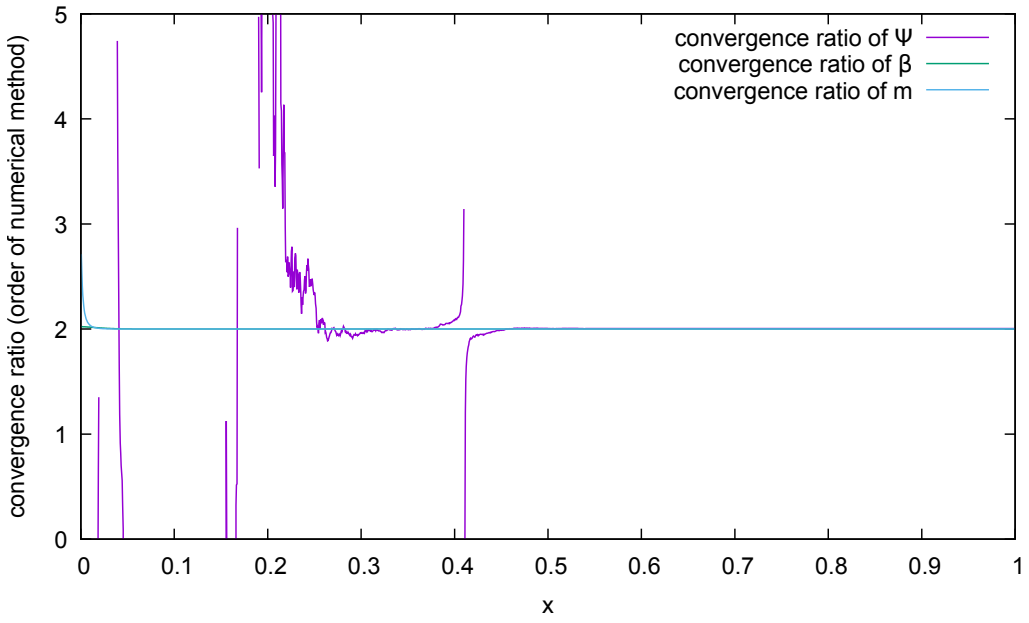

Figure 4.3: Convergence diagrams before the wave reached the origin.

4.2 Convergence for small time u

We repeat the same convergence test for a wave that has not yet reached the origin. We slice the grid at $u = const$. The convergence diagrams are shown below. The points near $x = 0$ are inconsistent with the rest of our figures. This can be easily explained. These points are in the area, where due to the gaussian fall-off of the inital data (see the Figure 3.16) no matter is present. This means no error in the calculations was made and both the denominator and the divisor in (4.5) are too close to zero to produce any meaningful results. Plot is shown in the Figure 4.3.

4.3 Testing with Einstein equations

As suggested in [1] we use the (u, u) and (u, r) component of the Einstein equations, which have to be satisfied, if our calculations are correct. We use a specific linear combination as suggested by [1], that is simple, while testing all quantities calculated before. Lets call out linear combination E_{uur}:

$$E_{uur} = 2e^{2\beta}\dot{m} + 8\pi\Big[\dot{\psi}^2 - e^{2\beta}\Big(\frac{1}{1-x} - \frac{2m}{x}\Big)(1-x)^2\dot{\psi}\Big(\psi_{,x}(1-x)\Big) - \frac{\psi}{x}\Big)\Big]. \quad (4.7)$$

If the equations are satifsied, $E_{uur} = 0$. We can follow [1] and use the normalization:

$$\mathbf{E_{uur}} = \frac{|E_{uur}|}{1 + max(E_{uur})}. \quad (4.8)$$

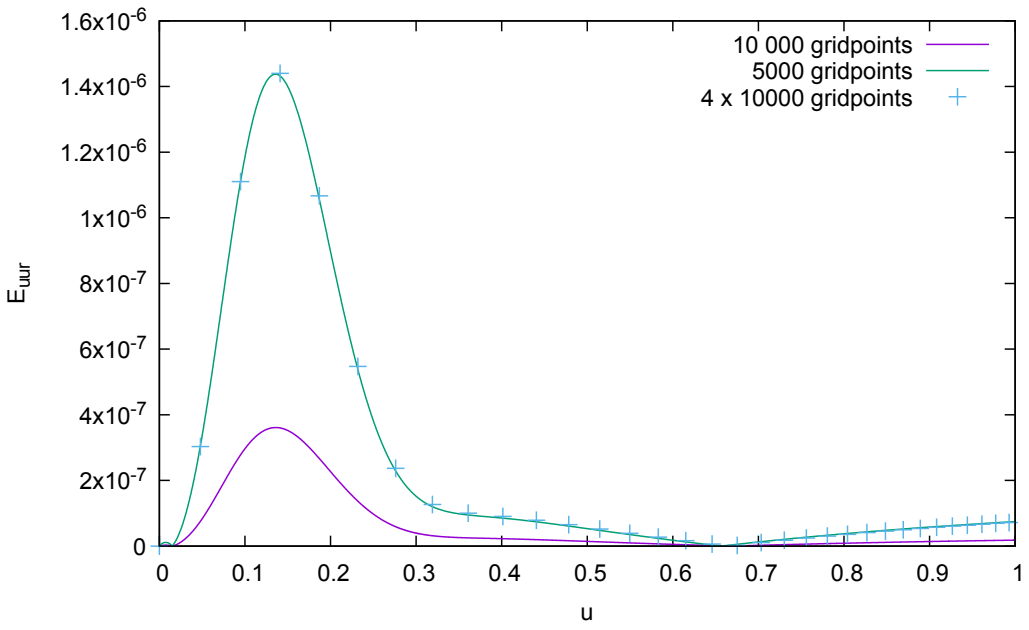

Figure 4.4: Convergence and values of E_{uur}. We can see another evidence that the algorithm is second order accurate.

Where $max(E_{uur})$ is the maximum of the absolute values of E_{uur} through the particular slice where the test is made. We can therefore say, that if the right-hand side of the equation equals zero the problem is solved correctly. The convergence diagram for E_{uur} at $u = 2.187$ is also done and shown in the Figure 4.4. We should note that if the methods are second order accurate, the E_{uur} should decrease four times when the grid is doubled.

5. Near-critical data

5.1 Behaviour for small p

Although we cannot expect any interesting behaviour with the weak-data evolution, it was used for convergence testing. It also gives us an insight on how the wave is drawn in our coordinate system. We are be using $p = 0.001 < 0.01p^*$. We let the system evolve and then plot the result in the Figure 5.1. We can notice

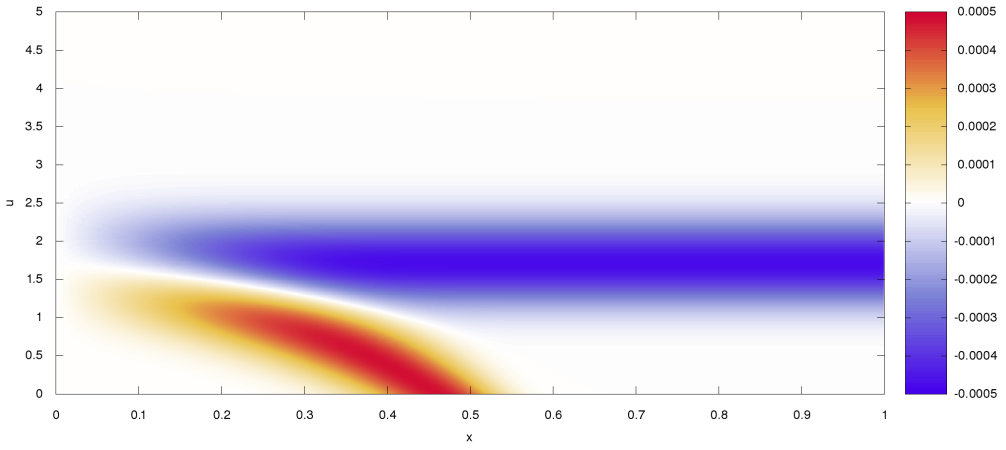

Figure 5.1: A wave evolution for the weak-data.

how the wave behaves in our coordinate system. Since we are working with a retarded time u, the wave is 'instantly' radiated to infinity, as soon as it reaches the origin $x = 0$. It is also deformed in x. This is because the further we are from $x = 0$, the larger distance is covered by a constant value Δx. Data at $\mathscr{I}^+$ show a nice gaussian-like shape without any distortion (see Figure 5.3). Practically we are observing a wave send to a center and then reflected to infinity without any observable deformations caused by the gravity of the the matter. The geodesics are not disturbed and are indistinguishable from those in flatspace. See them in the Figure 5.4. Finally, we can see how the Misner-Sharp function m behaves. This can be seen on 5.5.

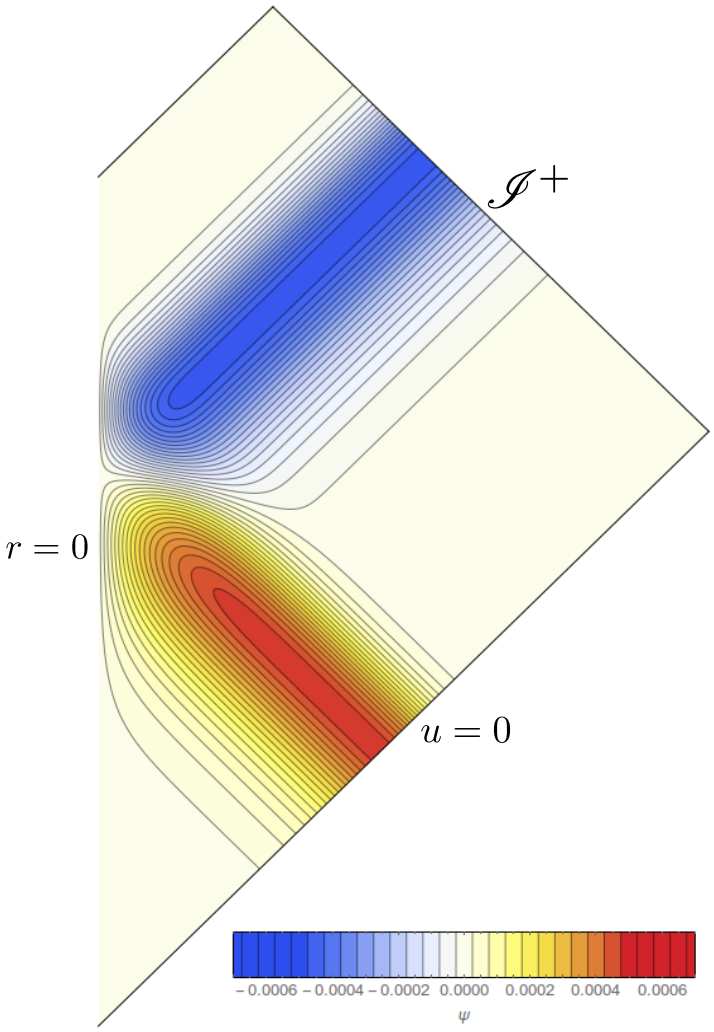

Figure 5.2: Carter-Penrose diagram for the weak wave. We can see the wave moves towards the center and then reflects to $\mathscr{I}^+$ without any visible deformations caused by the gravity. There is no event horizon present in the Figure. The simulation ends at the late time when the field disperses.

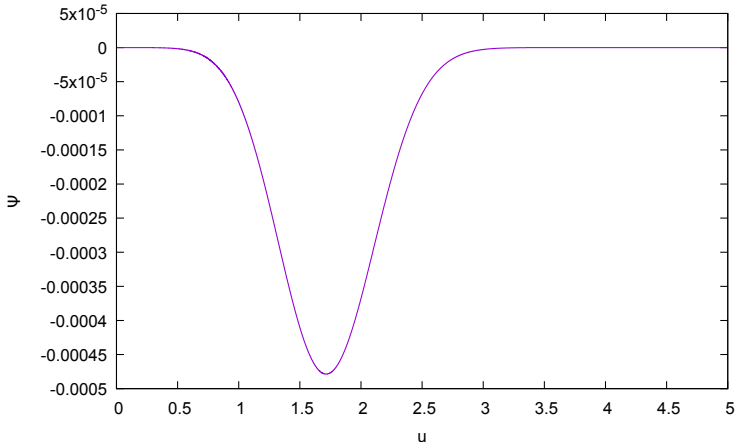

Figure 5.3: Wave $\psi(x=1,u)$ at $\mathscr{I}^+$ for weak-data.

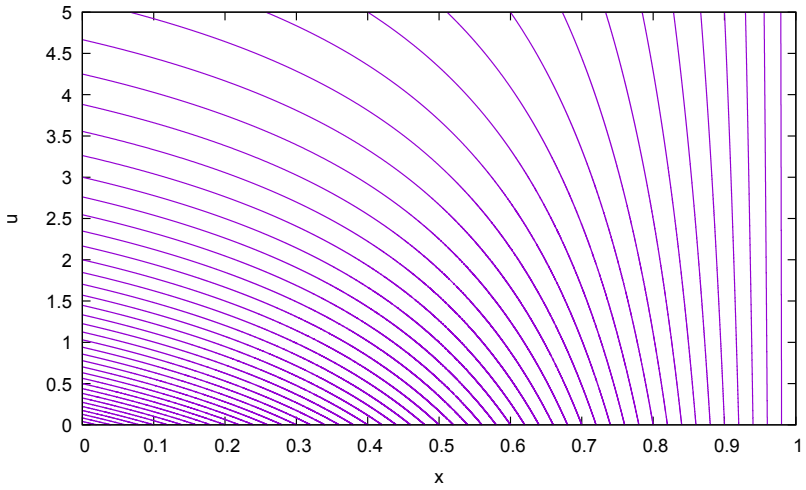

Figure 5.4: Radially infalling null geodesics for weak data.

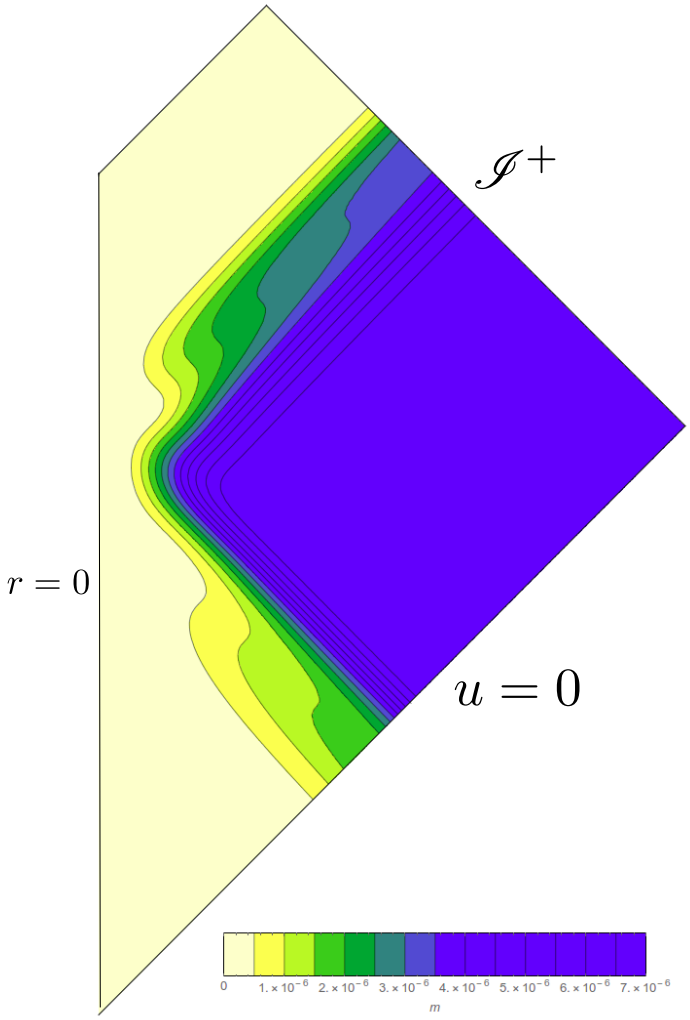

Figure 5.5: m in our spacetime for the weak data, showing the energy distribution in areas bounded by a sphere with radius x. We plot the Figure as a Carter-Penrose diagram, for we think it is more undestandable.

5.2 Above-critical evolution

In this section we will be observing the creation of a black hole. Our choice of coordinates does not allow us to cover the regions beyond the horizon. We only detect its presence by condition (3.18). At that moment we stop the simulation. The plot is pictured in the Figure 5.6. The simulation is stopped at

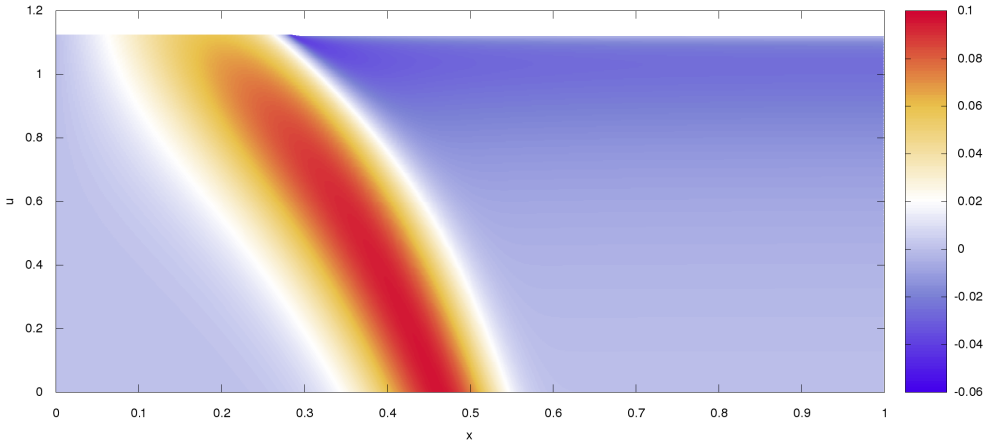

Figure 5.6: A wave evolution for the strong-data.

approximately $u \approx 1.1$ where a black hole is formed. The event is not visible on the Figure 5.6. However if we draw the geodesics we can see the increase in the density in one point - on the border of a newly formed black hole. 5.6. The shape of the wave at infinity displayed in the Figure 5.8 shows only the results of a nonlinearity of Einstein equations. A part of the wave is deflected on its own field and radiated to infinity.

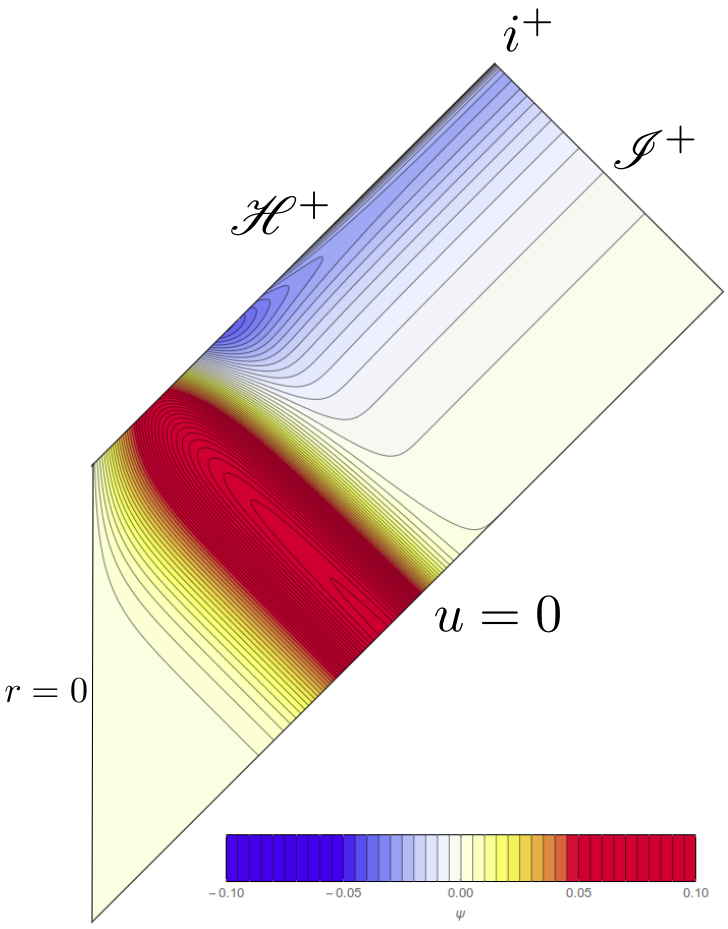

Figure 5.7: Carter-Penrose diagram for large p. We can see the event horizon $\mathscr{H}^+$ created before the main wave packet is reflected to infinity.

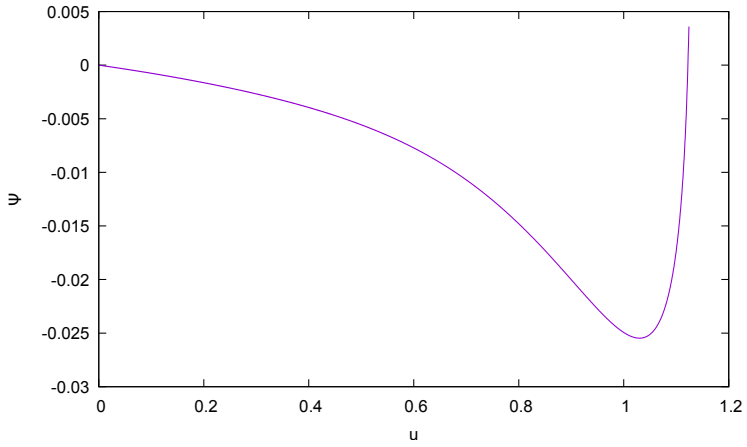

Figure 5.8: A wave at $\mathscr{I}^+$ for the strong-data.

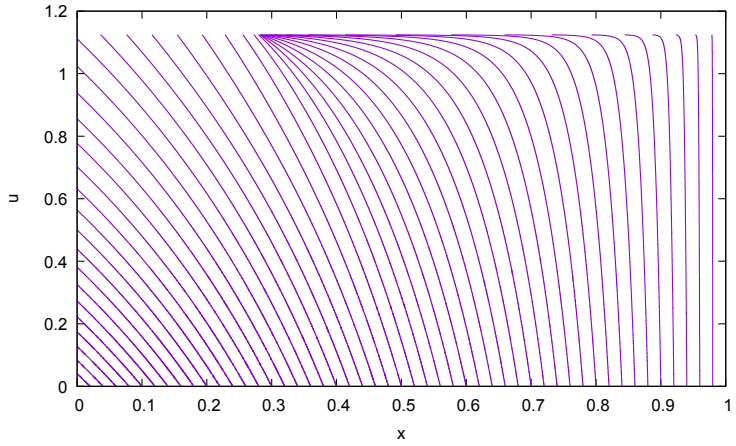

Figure 5.9: Radially infalling null geodesics for the strong-data.

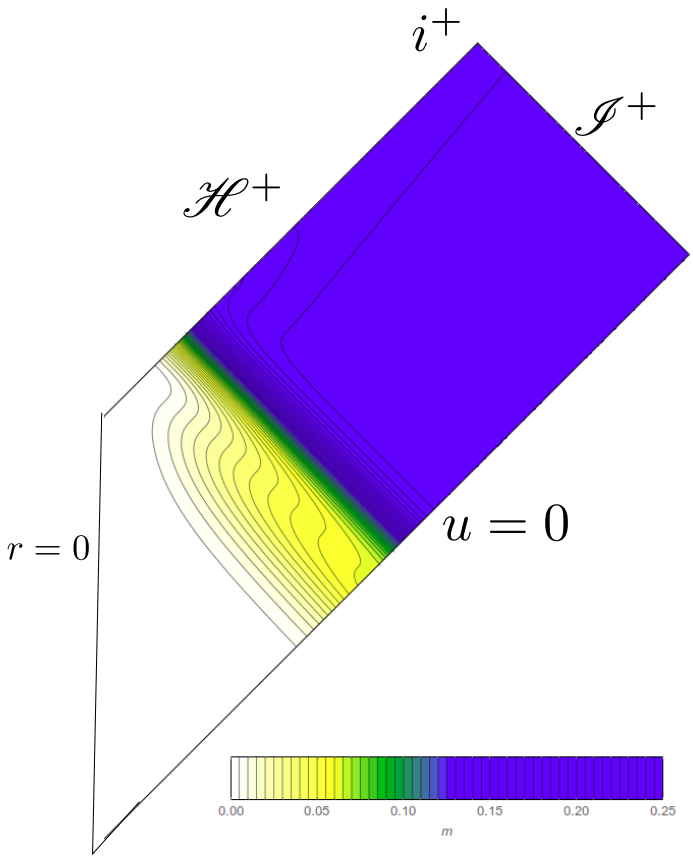

Figure 5.10: m in our spacetime for the strong data, showing the energy distribution in areas bounded by a sphere with radius x.

5.3 Near-critical evolution

The most interesting behaviour appears when we get close to the critical p^*. We have found an interval I where the critical p^* lies, with the length of I less than 10^{-10}. We have found the p^* to be between subrcitical p: $p_{sub} = 0.144930566102266$ and supercritical $p_{super} = 0.144930566176772$. In the next sections we are going to discuss the solution for upper (p_{super}) and lower (p_{sub}) bound of this interval.

5.3.1 Bisection search results

As described in the Chapter 3.5, the bisection search is run. We approach our critical $p*$ and get our subcritical and supercritical p-s during the process. As mentioned before, we have decided to watch the ratio of $2m/r$. Its dependence on the value of the parameter $p = A$ is in the Figure 5.11. To detect the collapse threshold we could also use the value of β at $\mathscr{I}^+$ as we can see in the Figure 5.12.

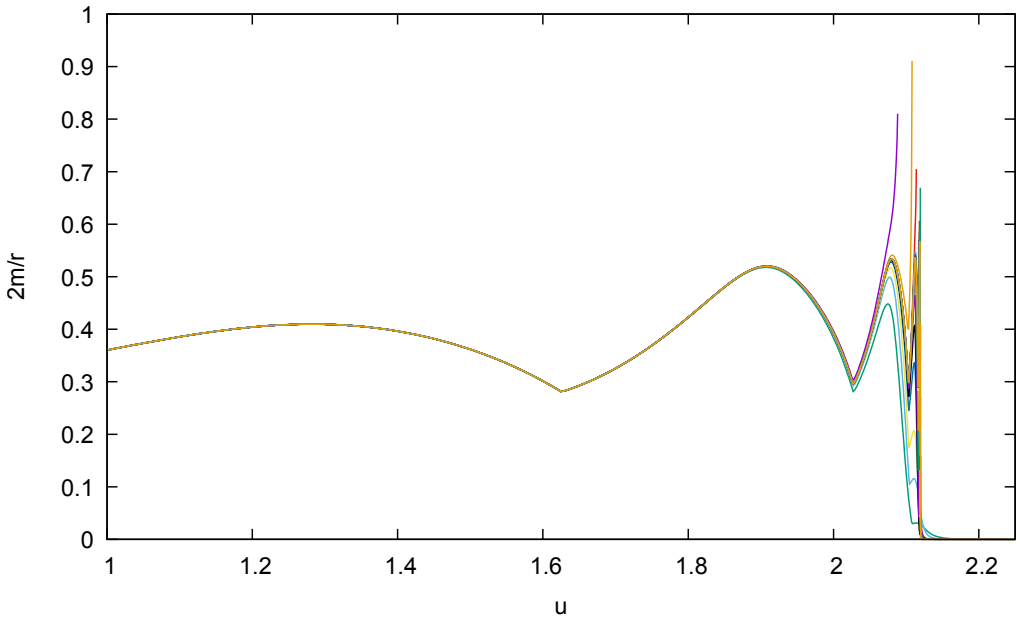

Figure 5.11: Evolution of 2m/r for various parameters p.

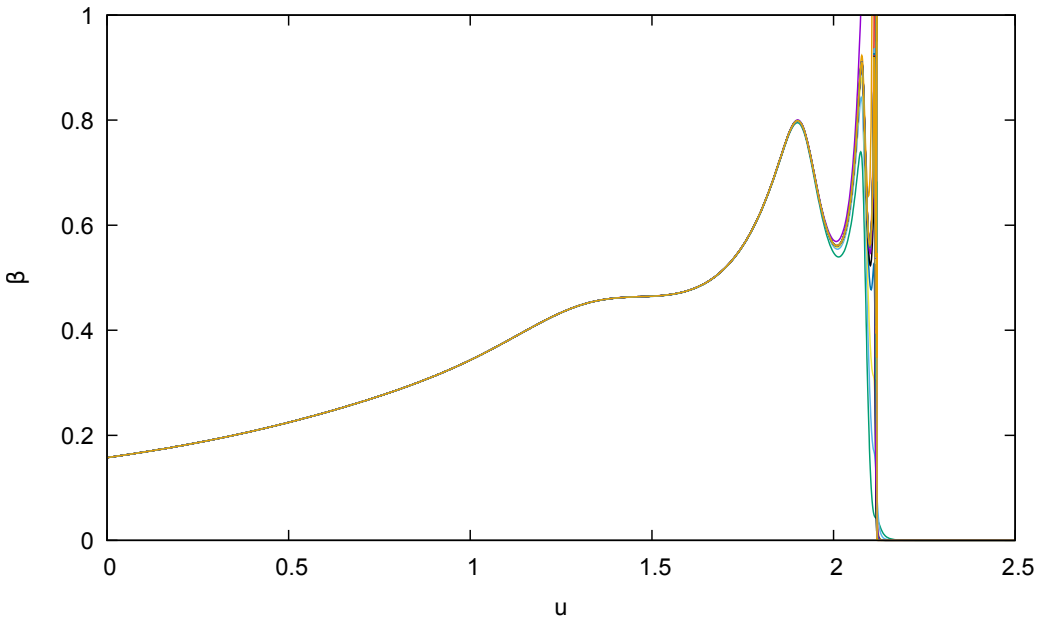

Figure 5.12: β at $\mathscr{I}^+$. The Figure is made using near-critical values of initial p. We can see the β shows oscilations, until it quickly falls to zero, or rises above one.

5.3.2 Below-critical solution

We can learn the most about the critical behaviour of a scalar field from the slightly subcritical evolution. A wave eventually dispersing and not creating a horizon means our simulation can continue as long as enough gridpoints are available. In the Figure 5.13 we can see the evolution of a system with p being the lower border of our interval I in other words previously mentioned p_{sub}. We can see in the Figure 5.15 the wave pattern echoing after the main wave have reached $\mathscr{I}^+$. This behaviour is better visible at wave profile at $\mathscr{I}^+$ (see the Figure 5.15).

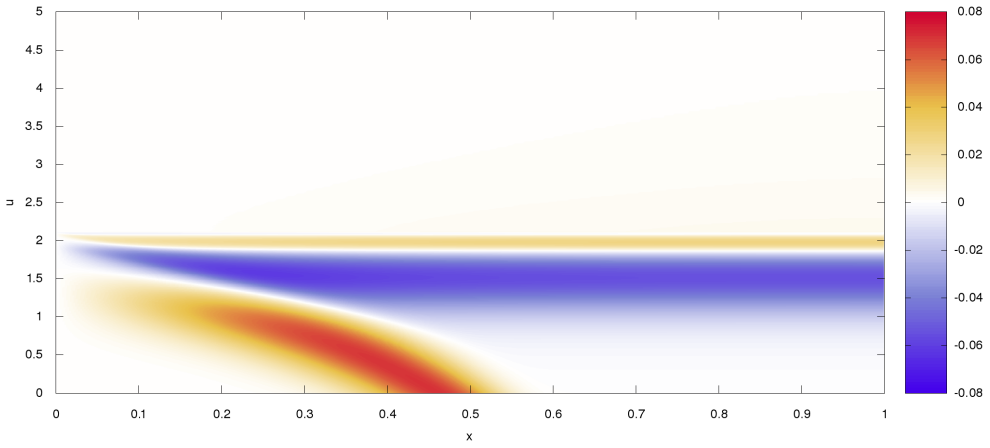

Figure 5.13: Evolution for slightly subcritical p.

Geodesics show a concentration close to the origin. When we compare it with the evolution in the Figure 5.13, we will see they are the most dense after the last echo is radiated out from the center. This means we are the closest to a black hole creation during the last echo we see. However as soon as the matter disperses, the geodesics return to the flatspace-like shape. The evolution of m can be seen in the Figure 5.17.

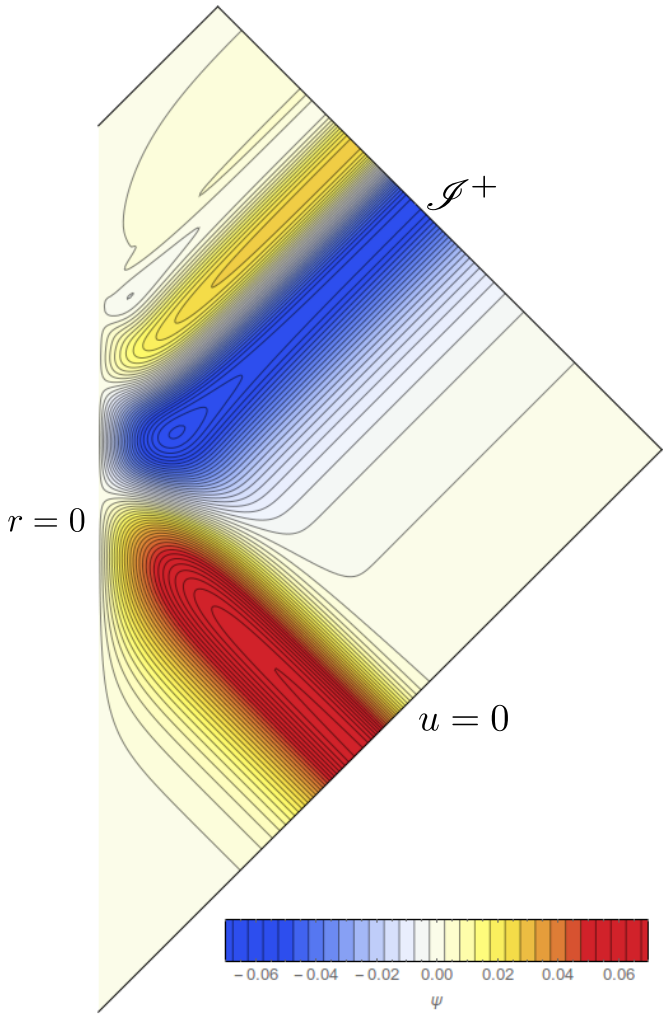

Figure 5.14: Carter-Penrose diagram for slightly subcritical p. Typical echoes are visible after the main wave is reflected to $\mathscr{I}^+$. There is no event horizon present in this Figure. The simulaton ends at the fixed time.

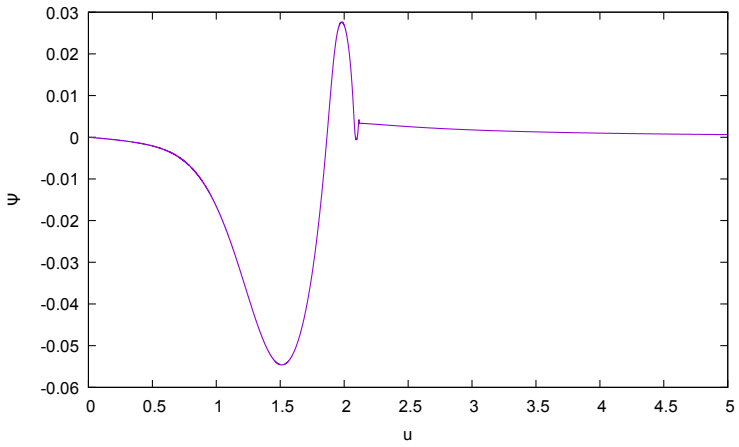

Figure 5.15: Wave at $\mathscr{I}^+$ for slightly subcritical p.

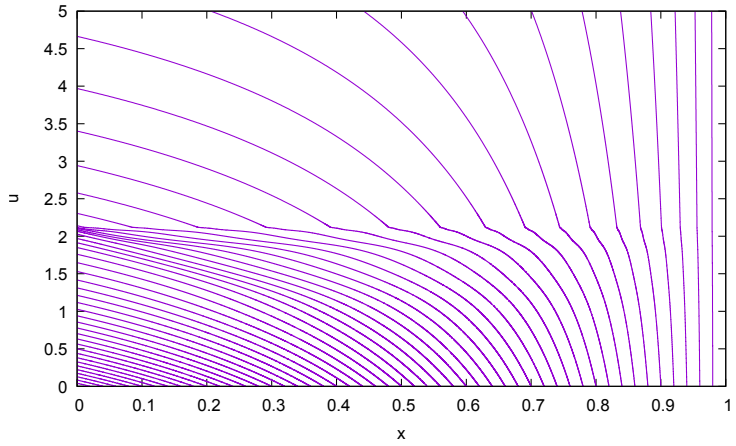

Figure 5.16: Radially infalling null geodesics for slightly subcritical p.

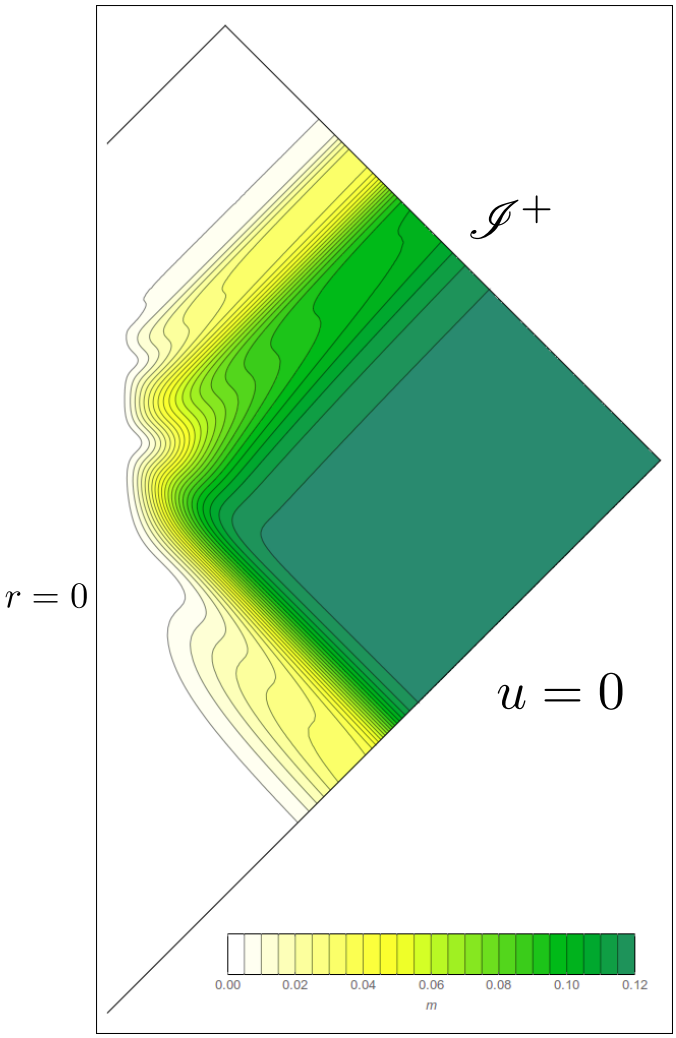

Figure 5.17: m in our spacetime for slightly subcritical p, showing the energy distribution in areas bounded by a sphere with radius x.

5.3.3 Above-critical solution

After we have introduced how a formation of a black hole looks in our coordinates (see the Chapter 5.2), we can proceed with the collapse for just slightly supercritical p. We are setting $p = p_{super}$. The simulation is stopped at he moment of black hole creation. The wave is plotted in the Figure 5.18

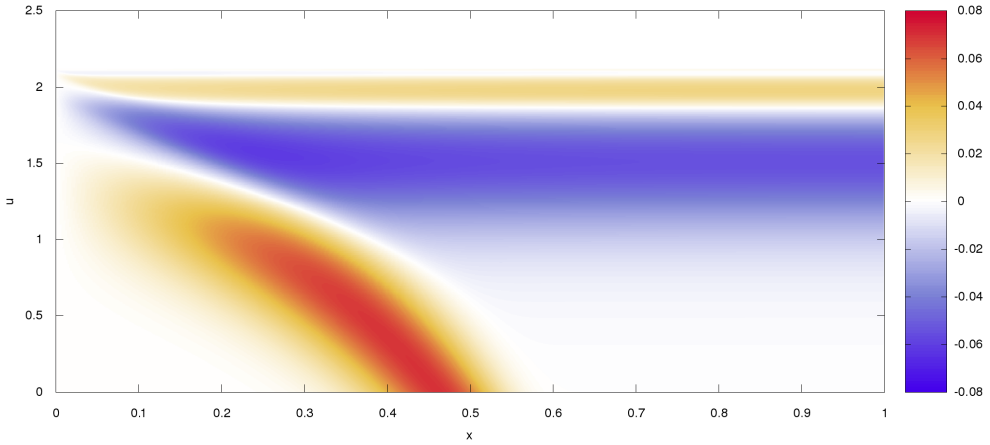

Figure 5.18: Evolution for slightly supercritical p.

The geodesics shown in the Figure 5.21 are concentrated much closer to the origin than in the case of strong data. This is because the black hole horizon is actually formed in the first point of our grid with non-zero x. The resulting black hole is therefore much smaller than in the case of the strong data. If we look in the Figure 5.13, we see that the black hole was created after the second echo. On the $\mathscr{I}^+$, however, we can see even more oscillations have reached $\mathscr{I}^+$. This leads us to a conclusion that black holes can be created after the main wave packet and eventually more of its echoes have reached the origin, meaning that lowering the parameter p lets more echos happen in the matter trapped at the center.

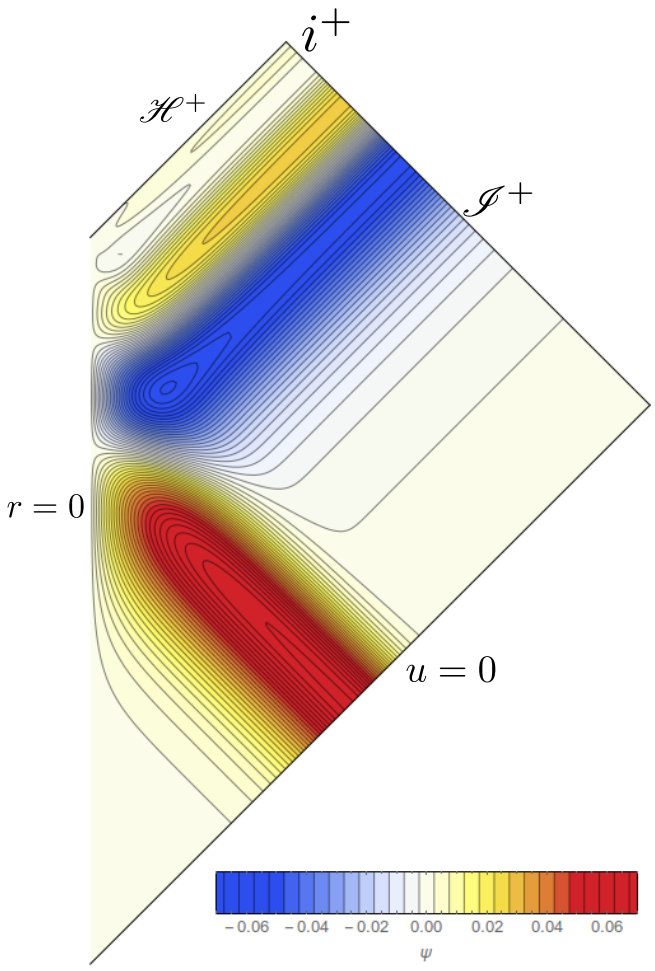

Figure 5.19: Carter-Penrose diagram for slightly supercritical p. The event horizon is created after the echoes are radiated to $\mathscr{I}^+$.

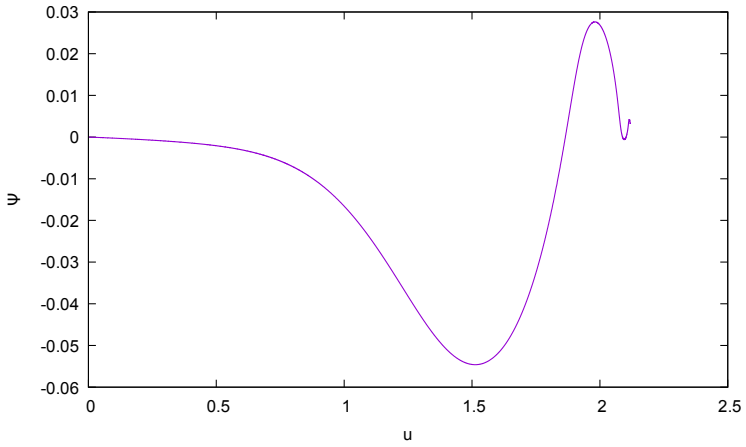

Figure 5.20: A wave at $\mathscr{I}^+$ for slightly supercritical p

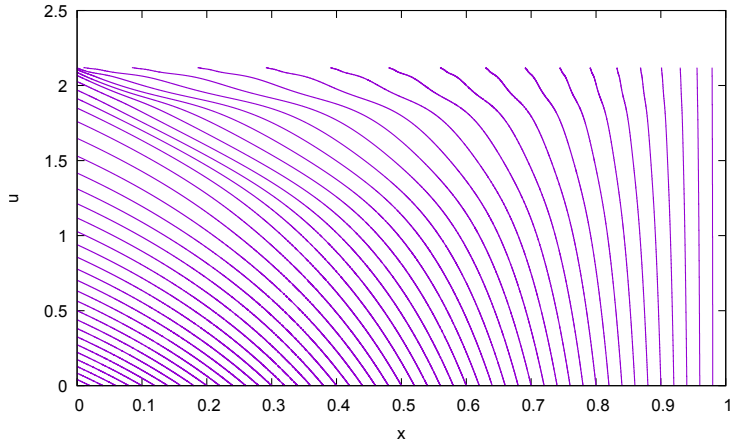

Figure 5.21: Radially infalling null geodesics for slightly supercritical p.

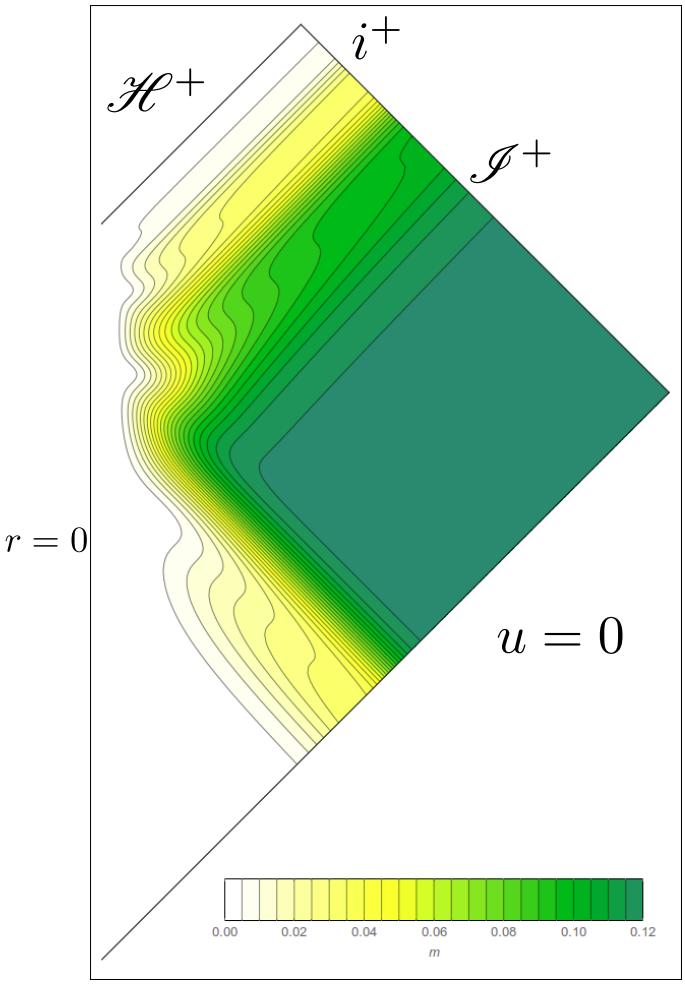

Figure 5.22: m in our spacetime for slightly supercritical p, showing the energy distribution in areas bounded by a sphere with radius x. For supercritical p most of the systems energy goes out through $\mathscr{I}^+$.

5.4 Phase diagram

In this section we will present our version of the phase diagram described in the Section 1.2. We have constructed our diagram using the retarded time u and the maximal values on the constant u slice of the functions $2m/r$ and $\frac{d\psi}{du}$. Data for these diagrams were gathered during the late stages of the bisection search, so that the near-critical values of the parameter p were used in plotting the Figure. A similar diagram was proposed by [12], but only a scheme is present in the article. Compare the figures 5.23 from [12] and 5.24.

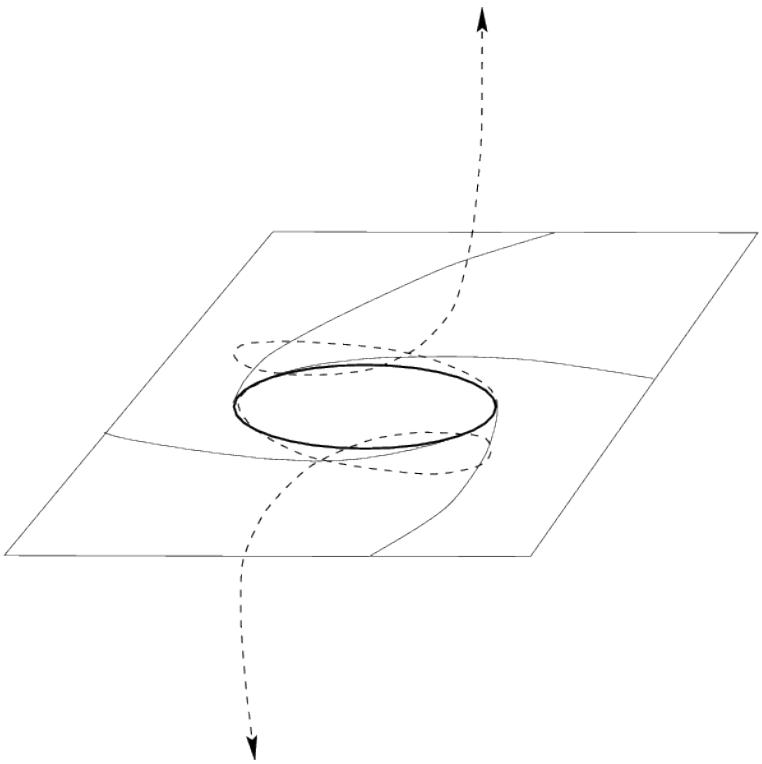

Figure 5.23: The proposed phase diagram from [12]. Black hole and flatspace attractors are above and below the critical hyperplain. The plain shown on the picture is composed of the points with the critical initial data. The critical point is shown not as a point but rather a circle.

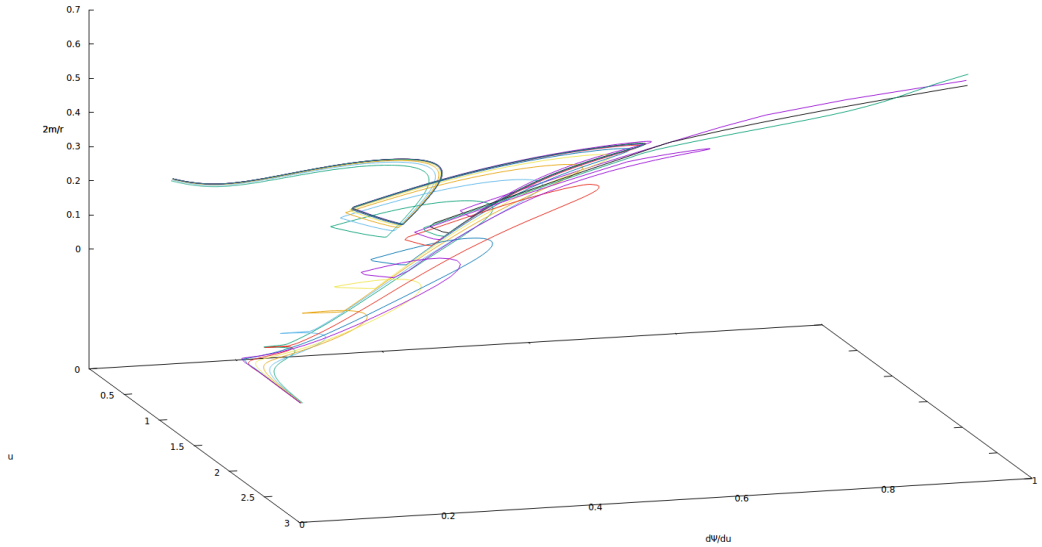

Figure 5.24: Our phase diagram for near-critical data. We can see the spiral at the beginning of the curve that eventually splits into more lines. We expect that the region with very dense lines can be an attractor of a critical state. The under-critical p-s end in the line with zero value of both $2m/r$ and β. The above-critical p-s end with $2m/r = 1$ and the derivative of ψ is more than one.

5.5 Self-similarity

We have mentioned the self-similarity in the section 1.2. For illustration we plot the value of $2m/r$, an important quantity representing a gravitational field strength in the spherical symmetry. The quantity is dimensionless, so we do not have to exponentially scale it. The Figure 5.26 nicely illustrates the self-similarity.

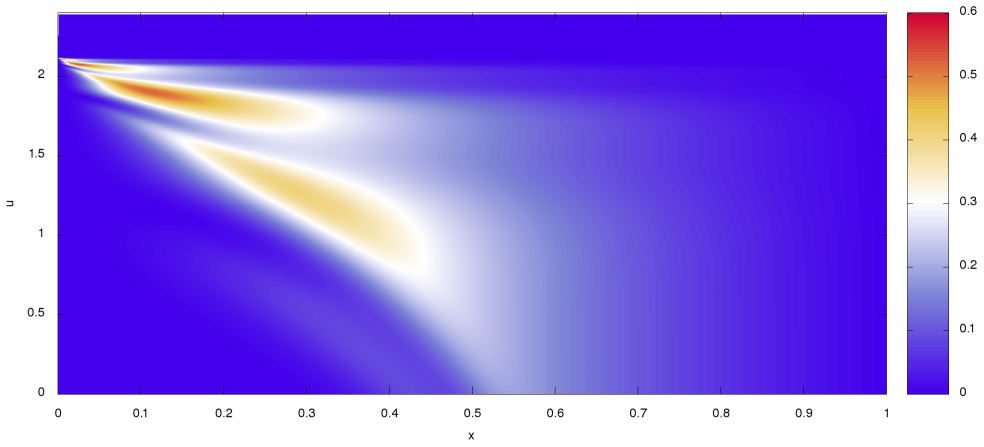

Figure 5.25: An illustration of the self-similarity for the slightly below-critical data in x, u system. The self-similarity is better visible on the Carter-Penrose (see Figure 5.26) diagram since no deformation caused by rotation affects the result and natural zooming feature is present.

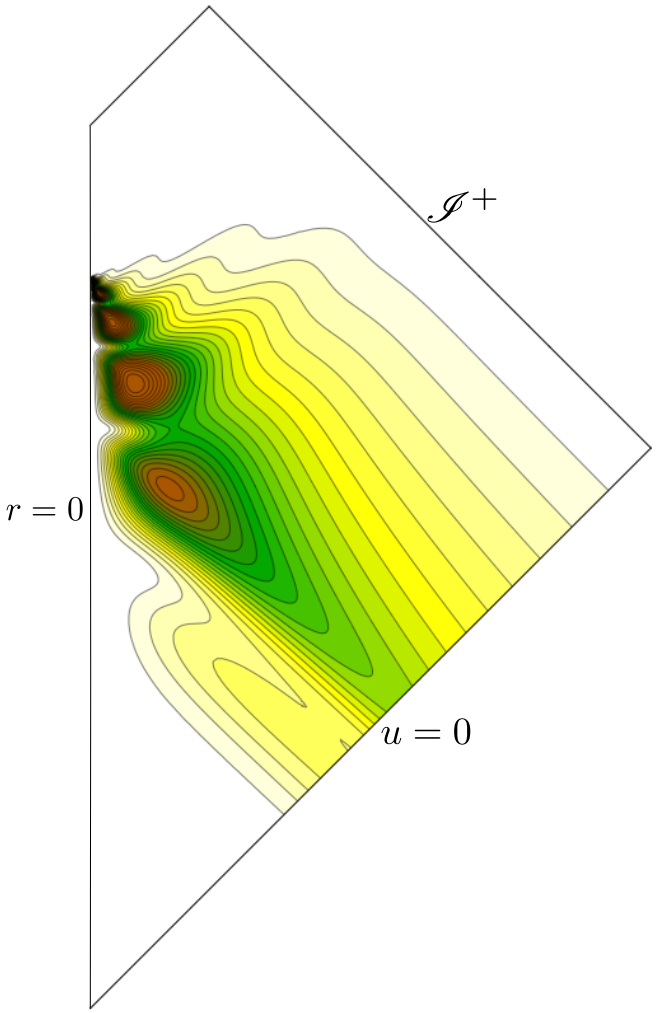

Figure 5.26: An illustration of the self-similarity for slightly below-critical data in a Carter-Penrose diagram. We can see the repeating pattern of the increasing $2m/r$. The maximum is closer to the center as the simulation continues. The property of C-P diagrams that radial null geodesic should be 45-degree lines does not at all determine a unique coordinate system we have to use. If U and V are null coordinates in such a diagram, $u' = f(U)$ and $v' = g(V)$ yield also a possible Carter-Penrose diagram. One can prefer coordinates which are linearly related to the central time or the time near $\mathscr{I}^+$. Here we use the coordinate $v'(u = 0) = x(u = 0)$ at $u = 0$ as the compactified advanced time and the simulation time as u'. As our simulation progresses more slowly near the cumulation point it naturally provides a kind of zooming into the central spacetime region so we can see the behaviour of the fields near $x = 0$ in more detail.

Conclusion

In this thesis we have studied the critical gravitational collapse of a scalar field in the spherical symmetry. First we have written and tested the program for weak amplitudes to understand the geometry, equations and wave behaviour. Then we have continued with finding the black hole formation threshold and afterwards we have extensively studied the subcritical and supercritical evolutions, the numerical methods used, the errors made during the calculations and the convergence in general.

We have analyzed the results and confirmed the findings of [1]. Next, we have tried to focus on the areas not covered in the article, such as the phase diagram described briefly in [8]. We have also studied the discrete self-similarity and presented the pictures showing how it looks like for certain quantities.

In the chapter about numerical methods: 3, we have described in detail what kind of methods did we use and their order of convergence. This can be helpful for others trying to simulate a wave in the spherical symmetry, since the numerical methods were mentioned only briefly in [1].

The chapter about the results themselves contains many figures to help the reader understand the concept of the coordinates used, the geodesics and the collapse in general.

Last but not least, the convergence test of our scheme is studied in 4. The main principle of the test used is derived in the beginning and many figures demonstrating how the results for our calculated data look like follow. The test with the remaining Einstein equations unused during the calculation process is an important part. It is a direct control of the results, possible to be used even during runtime.

The entire code used for calculations was written in C++, a language that, when used correctly, has good performance for numerical calculations. Figures are plotted using mainly Gnuplot: an open source computer program or using Wolfram Mathematica (for compactified figures).

List of Figures

1.1 A Penrose diagram of a collapse adapted from [1]. The green lines are $u = const$ slices of the constant retarded time u. We are using the retarded time also for our simulations. The blue lines represent $x = const$ hypersurfaces. $\mathscr{H}^+$ is the the event horizon. $\mathscr{I}^+$ serves as a symbol for the future null infinity that all null rays above the horizon reach, while $\mathscr{I}^-$ is the past null infinity. Singularity inside a black hole horizon is shown with the wavy line. The blue line $u = 0$ is where we set the initial data and let them evolve. 5

1.2 Phase diagram from [8]. The figure descibes expected trajectories in a phase space from a number of initial states. The curve made by varying p and keeping other parameter constant is marked. The point p^* is the black hole threshold, from which the system ends up in the critical point. The hyperplane representing all points that lead the evolution to the critical point is $\infty - 1$ dimensional and is also shown in the figure (as a 2D plane). The points representing black hole formation and flatspace are two other possible ending states for our system. A system having any initial data parameter non-critical necessarily ends in either of those two points, not in a critical state. 6

2.1 So-called marching algorithm for the wave equation. The value at vertex N is computed using (2.16) from already known values at E, S and W. This way the data at the new $u = const$ slice are obtained. 8

3.1 Flat-space null ingoing geodesics. 11

3.2 Profile of initial gaussian wave packet. Various initial data differ only by the amplitude A. 14

3.3 Values of metric functions beta and m in $u = 0$ slice. 15

3.4 Profile of the initial gaussian wave packet in terms of r coordinate. 16

3.5 Values of the metric functions beta and m in $u = 0$ slice in terms of r coordinate. 16

4.1 Wave profile at $\mathscr{I}^+$. 18

4.2 Convergence diagrams at $\mathscr{I}^+$. 18

4.3 Convergence diagrams before the wave reached the origin. 19

4.4 Convergence and values of E_{uur}. We can see another evidence that the algorithm is second order accurate. 20

5.1 A wave evolution for the weak-data. 21

5.2 Carter-Penrose diagram for the weak wave. We can see the wave moves towards the center and then reflects to $\mathscr{I}^+$ without any visible deformations caused by the gravity. There is no event horizon present in the Figure. The simulation ends at the late time when the field disperses. 22

5.3 Wave $\psi(x = 1, u)$ at $\mathscr{I}^+$ for weak-data. 22

5.4 Radially infalling null geodesics for weak data. 23

5.5 m in our spacetime for the weak data, showing the energy distribution in areas bounded by a sphere with radius x. We plot the Figure as a Carter-Penrose diagram, for we think it is more undestandable. 23
5.6 A wave evolution for the strong-data. 24
5.7 Carter-Penrose diagram for large p. We can see the event horizon $\mathscr{H}^+$ created before the main wave packet is reflected to infinity. . 25
5.8 A wave at $\mathscr{I}^+$ for the strong-data. 25
5.9 Radially infalling null geodesics for the strong-data. 26
5.10 m in our spacetime for the strong data, showing the energy distribution in areas bounded by a sphere with radius x. 26
5.11 Evolution of 2m/r for various parameters p. 27
5.12 β at $\mathscr{I}^+$. The Figure is made using near-critical values of initial p. We can see the β shows oscilations, until it quickly falls to zero, or rises above one. 28
5.13 Evolution for slightly subcritical p. 29
5.14 Carter-Penrose diagram for slightly subcritical p. Typical echoes are visible after the main wave is reflected to $\mathscr{I}^+$. There is no event horizon present in this Figure. The simulaton ends at the fixed time. 30
5.15 Wave at $\mathscr{I}^+$ for slightly subcritical p. 30
5.16 Radially infalling null geodesics for slightly subcritical p. 31
5.17 m in our spacetime for slightly subcritical p, showing the energy distribution in areas bounded by a sphere with radius x. 31
5.18 Evolution for slightly supercritical p. 32
5.19 Carter-Penrose diagram for slightly supercritical p. The event horizon is created after the echoes are radiated to $\mathscr{I}^+$. 33
5.20 A wave at $\mathscr{I}^+$ for slightly supercritical p 33
5.21 Radially infalling null geodesics for slightly supercritical p. 34
5.22 m in our spacetime for slightly supercritical p, showing the energy distribution in areas bounded by a sphere with radius x. For supercritical p most of the systems energy goes out through $\mathscr{I}^+$. . 34
5.23 The proposed phase diagram from [12]. Black hole and flatspace attractors are above and below the critical hyperplain. The plain shown on the picture is composed of the points with the critical initial data. The critical point is shown not as a point but rather a circle. 35
5.24 Our phase diagram for near-critical data. We can see the spiral at the beginning of the curve that eventually splits into more lines. We expect that the region with very dense lines can be an attractor of a critical state. The under-critical p-s end in the line with zero value of both $2m/r$ and β. The above-critical p-s end with $2m/r = 1$ and the derivative of ψ is more than one. 36
5.25 An illustration of the self-similarity for the slightly below-critical data in x, u system. The self-similarity is better visible on the Carter-Penrose (see Figure 5.26) diagram since no deformation caused by rotation affects the result and natural zooming feature is present. 37

5.26 An illustration of the self-similarity for slightly below-critical data in a Carter-Penrose diagram. We can see the repeating pattern of the increasing $2m/r$. The maximum is closer to the center as the simulation continues. The property of C-P diagrams that radial null geodesic should be 45-degree lines does not at all determine a unique coordinate system we have to use. If U and V are null coordinates in such a diagram, $u' = f(U)$ and $v' = g(V)$ yield also a possible Carter-Penrose diagram. One can prefer coordinates which are linearly related to the central time or the time near $\mathscr{I}^+$. Here we use the coordinate $v'(u = 0) = x(u = 0)$ at $u = 0$ as the compactified advanced time and the simulation time as u'. As our simulation progresses more slowly near the cumulation point it naturally provides a kind of zooming into the central spacetime region so we can see the behaviour of the fields near $x = 0$ in more detail. 38

Bibliography

[1] Michael Pürrer, Sascha Husa, and Peter C. Aichelburg. News from critical collapse: Bondi mass, tails, and quasinormal modes. *Phys. Rev. D*, 71:104005, May 2005.

[2] Wald M. Robert. *General relativity.* The University of Chicago Press, Chicago, 1984.

[3] Matthew W. Choptuik. Universality and scaling in gravitational collapse of a massless scalar field. *Phys. Rev. Lett.*, 70:9–12, Jan 1993.

[4] Tatsuhiko Koike, Takashi Hara, and Satoshi Adachi. Critical behavior in gravitational collapse of a perfect fluid. *Phys. Rev. D*, 59:104008, Apr 1999.

[5] Carsten Gundlach and José M. Martín-García. Charge scaling and universality in critical collapse. *Phys. Rev. D*, 54:7353–7360, Dec 1996.

[6] Matthew W. Choptuik, Eric W. Hirschmann, Steven L. Liebling, and Frans Pretorius. Critical collapse of the massless scalar field in axisymmetry. *Phys. Rev. D*, 68:044007, Aug 2003.

[7] Thomas W. Baumgarte and Carsten Gundlach. Critical collapse of rotating radiation fluids. *Phys. Rev. Lett.*, 116:221103, Jun 2016.

[8] Carsten Gundlach. Critical phenomena in gravitational collapse. *Living Reviews in Relativity*, 2(1):4, 1999.

[9] H. BONDI. Gravitational waves in general relativity. *Nature*, 186(4724):535–535, May 1960.

[10] R. Gómez and J. Winicour. Asymptotics of gravitational collapse of scalar waves. *Journal of Mathematical Physics*, 33(4):1445–1457, 1992.

[11] Charles W. Misner and David H. Sharp. Relativistic equations for adiabatic, spherically symmetric gravitational collapse. *Phys. Rev.*, 136:B571–B576, Oct 1964.

[12] Carsten Gundlach. Understanding critical collapse of a scalar field. *Phys. Rev. D*, 55:695–713, Jan 1997.